

NATIONAL AERONAUTICS AND SPACE ADMINISTRATION

*Technical Memorandum 33-796*

*Optical Guidance Vidicon Test Program  
Final Report*

(NASA-CR-148834) OPTICAL GUIDANCE VIDICON  
TEST PROGRAM Final Report. (Jet Propulsion  
Lab.) 68 p HC \$4.50

N76-34097

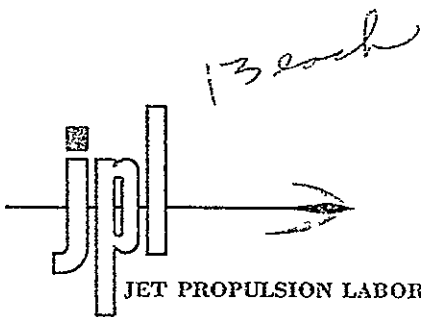
CSCL 03B

Unclassified  
G3/91. 07972

JET PROPULSION LABORATORY  
CALIFORNIA INSTITUTE OF TECHNOLOGY  
PASADENA, CALIFORNIA

September 15, 1976





JET PROPULSION LABORATORY California Institute of Technology • 4800 Oak Grove Drive, Pasadena, California 91103

29 October 1976

NASA Scientific and Technical  
Information Facility  
P. O. Box 8757  
Baltimore-Washington International Airport  
Maryland 21240

Attention: NASA Representative (S-AK-RKT)

Gentlemen:

Attached herewith are COSATI Technical Report Standard Title Pages for JPL Technical Documents released during September 1976.

1. TM 33-734 Mariner Venus-Mercury 1973 Project Final Report  
Vol. 1 Venus and Mercury I Encounters
2. TM 33-785 Disturbing Effects of Attitude Control Maneuvers on the Orbital Motion of the Helios Spacecraft
3. TM 33-787 Final Report: Apollo Experiment S-217 IR/Radar Study of Apollo Data
4. TM 33-791 System Design for a Nuclear Electric Spacecraft Utilizing Out-of-Core Thermionic Conversion
5. TM 33-792 Advanced Multilateration Theory, Software Development, and Data Processing: The MICRDOT System
6. TM 33-793 Large-Payload Earth-Orbit Transportation with Electric Propulsion
- ✓7. TM 33-796 Optical Guidance Vidicon Test Program Final Report
8. SP 43-36 Determination of the Cosmological Rate of Change of G and the Tidal Accelerations of Earth and Moon from Ancient and Modern Astronomical Data

Copies of the following reports, for which Standard Title Pages are enclosed, were released to NASA for unrestricted systems input and announcement at the time of initial distribution:

1. TR 32-1606 Sustained Load Crack Growth Design Data for TI-6AI-4V Titanium Alloy Tanks Containing Hydrazine
2. Biblio Publications of the Jet Propulsion Laboratory:  
39-17 January Through December 1975

*13 Oct*  
JET PROPULSION LABORATORY California Institute of Technology 4800 Oak Grove Drive, Pasadena, California 91103

NASA STIF

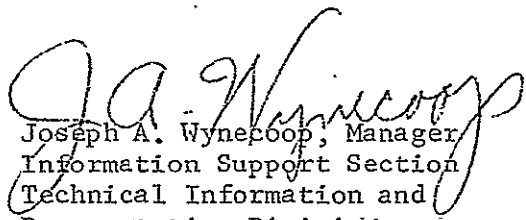
- 2 -

10/29/76

Two copies of the following JPL Civil Systems Project Office documents are enclosed for your systems input and listing in the unlimited, unclassified category of STAR if desired.

1. JPL 5101-3 LSSA Low-Cost Silicon Solar Array Project  
First Annual Report
2. JPL 5101-7 LSSA Low-Cost Silicon Solar Array Project  
Project Quarterly Report-1

Very truly yours,

  
Joseph A. Wynecoop, Manager  
Information Support Section  
Technical Information and  
Documentation Division

JAW/GAM:gb

Enclosures

## HOW TO FILL OUT THE TECHNICAL REPORT STANDARD TITLE PAGE

Make items 1, 4, 5, 9, 12, and 13 agree with the corresponding information on the report cover. Use all capital letters for title (item 4). Leave items 2, 6, and 14 blank. Complete the remaining items as follows:

3. Recipient's Catalog No. Reserved for use by report recipients.
7. Author(s). Include corresponding information from the report cover. In addition, list the affiliation of an author if it differs from that of the performing organization.
8. Performing Organization Report No. Insert if performing organization wishes to assign this number.
10. Work Unit No. Use the agency-wide code (for example, 923-50-10-06-72), which uniquely identifies the work unit under which the work was authorized. Non-NASA performing organizations will leave this blank.
11. Insert the number of the contract or grant under which the report was prepared.
15. Supplementary Notes. Enter information not included elsewhere but useful, such as: Prepared in cooperation with... Translation of (or by)... Presented at conference of... To be published in...
16. Abstract. Include a brief (not to exceed 200 words) factual summary of the most significant information contained in the report. If possible, the abstract of a classified report should be unclassified. If the report contains a significant bibliography or literature survey, mention it here.
17. Key Words. Insert terms or short phrases selected by the author that identify the principal subjects covered in the report, and that are sufficiently specific and precise to be used for cataloging.
18. Distribution Statement. Enter one of the authorized statements used to denote releasability to the public or a limitation on dissemination for reasons other than security of defense information. Authorized statements are "Unclassified—Unlimited," "U. S. Government and Contractors only," "U. S. Government Agencies only," and "NASA and NASA Contractors only."
19. Security Classification (of report). NOTE: Reports carrying a security classification will require additional markings giving security and downgrading information as specified by the Security Requirements Checklist and the DoD Industrial Security Manual (DoD 5220.22-M).
20. Security Classification (of this page). NOTE: Because this page may be used in preparing announcements, bibliographies, and data banks, it should be unclassified if possible. If a classification is required, indicate separately the classification of the title and the abstract by following these items with either "(U)" for unclassified, or "(C)" or "(S)" as applicable for classified items.
21. No. of Pages. Insert the number of pages.
22. Price. Insert the price set by the Clearinghouse for Federal Scientific and Technical Information or the Government Printing Office, if known.

## TECHNICAL REPORT STANDARD TITLE PAGE

1. Report No. 33-796	2. Government Accession No.	3. Recipient's Catalog No.	
4. Title and Subtitle  OPTICAL GUIDANCE VIDICON TEST PROGRAM FINAL REPORT		5. Report Date September 15, 1976	6. Performing Organization Code
7. Author(s) Allan R. Eisenman, Richard H. Stanton, Charles C. Voge		8. Performing Organization Report No.	
9. Performing Organization Name and Address  JET PROPULSION LABORATORY California Institute of Technology 4800 Oak Grove Drive Pasadena, California 91103		10. Work Unit No.	11. Contract or Grant No. NAS 7-100
		13. Type of Report and Period Covered  Technical Memorandum	14. Sponsoring Agency Code
12. Sponsoring Agency Name and Address  NATIONAL AERONAUTICS AND SPACE ADMINISTRATION Washington, D.C. 20546		15. Supplementary Notes  -	
16. Abstract  A laboratory and field test program was conducted to quantify optical-navigation parameters of Mariner vidicons. A scene simulator and a camera were designed and built for vidicon tests under a wide variety of conditions. Laboratory tests characterized error sources important to the optical-navigation process and field tests verified star sensitivity and characterized comet optical guidance parameters. The equipment, tests and data reduction techniques used are described. Key test results are listed. A substantial increase in the understanding of the use of selenium vidicons as detectors for spacecraft optical guidance was achieved, indicating a reduction in residual offset errors by a factor of two to four to the single pixel level.			
17. Key Words (Selected by Author(s))  Electronics and Electrical Engineering Optics Lunar and Planetary Exploration (Advanced) Mariner Jupiter/Saturn 1977 Project		18. Distribution Statement  Unclassified -- Unlimited	
19. Security Classif. (of this report)  Unclassified	20. Security Classif. (of this page)  Unclassified	21. No. of Pages 68	22. Price

NATIONAL AERONAUTICS AND SPACE ADMINISTRATION

*Technical Memorandum 33-796*

*Optical Guidance Vidicon Test Program  
Final Report*

*Allan R. Eisenman*

*Richard H. Stanton*

*Charles C. Voge*

JET PROPULSION LABORATORY  
CALIFORNIA INSTITUTE OF TECHNOLOGY  
PASADENA, CALIFORNIA

September 15, 1976

Prepared Under Contract No NAS 7-100  
National Aeronautics and Space Administration

## PREFACE

The facilities and field tests for the Optical Guidance Vidicon Test Program were funded by the Optical Guidance Data Laboratory task of the Advanced Navigation Research and Technology Operating Plan (RTOP). The laboratory tests and this report were co-sponsored by the Optical Guidance Data Laboratory and the Mariner Jupiter/Saturn 1977 (MJS'77) Project at the Jet Propulsion Laboratory.

#### ACKNOWLEDGMENTS

The authors gratefully acknowledge the work of others who made this program possible: W. Breckenridge for general guidance and for assistance with his ODCR processing; H. Primus for test-set design contributions, construction, and check out; W. Goss for simulator design; and J. Miller for tape decoding.

## CONTENTS

### SECTION

I.	SUMMARY . . . . .	1
II.	INTRODUCTION . . . . .	5
III.	TEST DESCRIPTION . . . . .	7
	A. Vidicon Test Set . . . . .	7
	B. Test Set Operations. . . . .	8
	C. Test Set Block Diagram . . . . .	9
	D. Laboratory Description . . . . .	12
	E. Scene Simulator Calibration Equipment and Description. . . . .	14
	F. Video Data Processing. . . . .	16
	1. Optical Data Calibration and Rectification (ODCR) Program. . . . .	17
	2. Image Processing Program (IMP). . . . .	19
	3. Image Plane Measurements. . . . .	21
	4. Vidicon Calibration Using Reseaux . . . . .	21
	5. Data Flow . . . . .	22
IV.	FIELD TESTS. . . . .	23
	A. Photometric Calibration. . . . .	23
	B. Comet Measurements . . . . .	28
V..	LABORATORY TEST RESULTS. . . . .	35
	A. Simulator Image Calibration Accuracy . . . . .	35
	B. Star-Image Centerfinding Accuracy. . . . .	40
	C. Target/Star Measurement. . . . .	46
	D. Summary. . . . .	55
VI.	DIRECTIONS FOR FUTURE WORK . . . . .	57
REFERENCES	. . . . .	59
APPENDIX A	TEST-SET OPERATIONAL CONTROLS. . . . .	61
APPENDIX B	FIELD-TEST FRAMES. . . . .	65

## TABLES

1.	Sample star-image centerfinding results . . . . .	43
----	---	----

## ILLUSTRATIONS

1.	Star Transfer Characteristics for Laboratory Simulated Star Images . . . . .	9
2.	Optical Guidance Data Laboratory (OGDL) Test Camera Head Block Diagram . . . . .	10
3.	OGDL Test Camera Controller/Recorder Block Diagram . . . . .	11
4.	Laboratory Set-Up Optical Scene Simulator With Selenium Vidicon Camera . . . . .	13
5.	Scene Simulator Configuration . . . . .	14
6.	Scene Simulator Calibration Equipment . . . . .	15
7.	Pseudo Spacecraft Coordinates . . . . .	18
8.	Typical Disk Limb Profiles (Range of contour levels used for center findings shown) . . . . .	20
9.	Laboratory Measurement Data Flow . . . . .	22
10.	Field Test Camera and Tracking Telescope . . . . .	24
11.	Double Star Image from Field Test . . . . .	25
12.	Calculated Star Color Correction for Mariner Vidicons . . . . .	26
13.	Field Test Star Sensitivity of Test Camera . . . . .	27
14.	Comet Bradfield Test Frame Exposure = 10 min . . . . .	29
15.	Exposure Required for Detection (MVM camera-seconds) . . . . .	30
16.	Image Contour Plot-Comet Bradfield . . . . .	32
17.	Comet Bradfield Image (Five pixel ave.) . . . . .	33
18.	Calibration Equipment X-Axis Correction . . . . .	36
19.	Calibration Equipment Y-Axis Correction . . . . .	36
20.	Center-Star Top Profile . . . . .	37
21.	Clear Disk Image - Edge Profile . . . . .	37
22.	Image Plane Intensity Traverse for 30° Phase Angle Target . . . . .	38
23.	Pixel Printout of Top Edge of a Bright Clear Disc (FN100) . . . . .	40

## ILLUSTRATIONS (contd)

24.	Pixel Printouts of a Typical Star as a Function of Intensity . . . . .	41
25.	Contours of a Typical Star as a Function of Intensity . . . . .	42
26.	Star Image Motion vs Brightness . . . . .	44
27.	4-Level Line Offset vs Star Brightness . . . . .	45
28.	Target Body Motion vs Exposure (Target center found using "high" intensity contour (Section II)) . . . . .	48
29.	Target Body Motion vs Exposure (Pixel direction) . . . . .	49
30.	Target Body Shift vs Exposure (Low contours) . . . . .	50
31.	Reseau Motion Due to Heavily Overexposed (50x) Disk Image (Normal background level) . . . . .	52
32.	Reseau Motion Due to Heavily Overexposed (90x) Disk Image with 38% Background Light Flood . . . . .	52
33.	Typical Reseau Image Against Weak Background . . . . .	53
34.	Reseau Image with 10% Background Light Flood . . . . .	54
35.	Reseau and Disk Image Motion vs Exposure . . . . .	54

## ABSTRACT

A laboratory and field test program was conducted to quantify optical-navigation parameters of Mariner vidicons. A scene simulator and a camera were designed and built for vidicon tests under a wide variety of conditions. Laboratory tests characterized error sources important to the optical-navigation process and field tests verified star sensitivity and characterized comet optical guidance parameters. The equipment, tests and data reduction techniques used are described. Key test results are listed. A substantial increase in the understanding of the use of selenium vidicons as detectors for spacecraft optical guidance was achieved, indicating a reduction in residual offset errors by a factor of two to four to the single pixel level.

SECTION I  
SUMMARY

The power of optical measurements for navigation has been demonstrated on flight missions. These demonstrations proved the feasibility of the optical-navigation concept, but the flight data left many questions unanswered. It was not possible to determine measurement bias errors to the required desirable level of a single TV-pixel. It was not possible to obtain parametric information on the effects of variations in target size, brightness and phase angle because of operational constraints and restricted geometry. Finally, the flight experience provided no data on comets, where optical navigation is likely to play a key mission role.

Because of these limitations a laboratory and field test program was initiated to quantify optical-navigation measurement parameters of Mariner vidicons. This program was part of a continuing technology development for a variety of future missions such as Mariner Jupiter/Saturn 1977. In support of this development, a scene simulator was built which projected realistic star and target images onto a reference image plane. A test camera consisting of a sensor head, control electronics and a tape recorder was built which permitted vidicons to be operated under a variety of test conditions. Then software elements were assembled from previous optical navigation flight demonstrations and ongoing software development programs. The resulting test system made it possible to accurately simulate a desired target/star geometry on the vidicon faceplate, encode and store the resulting video data on magnetic tape, and, finally, feed the video data through the measurement-extraction software. The final positional measurements were then compared to those generated with the optical simulator, which itself was calibrated with an accurate microradiometer.<sup>1</sup>

---

<sup>1</sup>

Much of this equipment, particularly the optical simulator, is applicable to characterization of sensors other than vidicons and will soon be applied to solid state imagers..

Data generated through this procedure permitted detailed tests of error sources important to the optical-navigation measurement process. The effect of target body overexposure on centerfinding accuracy is an error-source example as are star image centerfinding accuracy and the effect of background stray light, which were also investigated.

A second phase of the vidicon test program involved field tests on astronomical targets. Although field measurements have obvious disadvantages (e.g., atmospheric effects must be taken into account), a number of the available targets (moon, planets, star clusters, comets, etc.) provided excellent calibration sources. By imaging stars, it was possible to verify that the test vidicon had essentially the same sensitivity as that used on Mariner 10. It was also possible, by photographing comet Bradfield (1974), to provide quantitative exposure data for optical navigation on comet missions.

Key test results are:

1. It is possible to calibrate all the effects of star offsets to obtain star to star accuracies of 0.1 TV lines.
2. Star image offsets in the pixel direction are negligible.
3. There is a minimum clear disk target body offset of about one line at the lowest levels of exposure.
4. The total clear disk target body offset can be calibrated to better than one element over an exposure range from 2% to 9000% of full scale.
5. Partial background light flooding (4 to 10%) should be used to improve reseau detection, to reduce beam bending errors and to improve star detectability (previously demonstrated).
6. The diffuse nature of comets reduces detectability by several magnitudes.
7. Comet centerfinding can approach the accuracy of clear disk centerfinding if new software is developed for this purpose.

In conclusion, it was found that the combination of field and laboratory tests has furnished a substantial working knowledge of selenium vidicon characteristics when used for optical navigation, indicating a reduction in residual offset errors by a factor of 2 to 4 to the one pixel level.

As optical navigation moves into the realm of mission critical technology, new imaging sensors are emerging which offer substantial promise for target/star imaging. Of particular interest are the new solid state imagers. A variety of charge coupled devices (CCD) and charge injection devices (CID) are being developed, offering substantially improved performance in sensitivity, dynamic range, and geometric accuracy. For this reason, future emphasis in the Optical Guidance Laboratory will be directed toward quantitatively measuring the performance of these new sensors for optical navigation, target body tracking, and, ultimately, for use in an autonomous guidance and navigation system.

SECTION II  
INTRODUCTION

Flight demonstrations of optical-navigation have been made during the Mariner Mars 1969 and 1971 missions (Refs. 1, 2, 3). However, the resulting overall accuracy was limited. In 1969 it was shown that improved trajectory estimates could be achieved by optically tracking Mars during the approach phase of the mission. In 1971, greater accuracy was demonstrated by tracking the Martian satellite Deimos, and using background stars to provide coordinate references. Finally, the flight of Mariner 10 to Venus and Mercury successfully demonstrated (Refs. 4, 5) optical navigation measurements with a large, bright target body (Mercury) and one background star. Good reproducibility was demonstrated in the measurements despite some problems with the video data and the necessity of tracking a target over  $10^5$  times brighter than the background reference stars.

The optical-navigation process involves the apparent direction vector to a target body (planet, satellite, comet, etc.) with respect to background stars and using this information in the trajectory-estimation process. Onboard measurements can lead directly to improved trajectory accuracy, improved instrument pointing, and reduction in trajectory-correction, fuel-loading requirements. Stringent accuracy demands are often placed on the measurements to meet mission requirements in all of these areas which resulted in the initiation of a laboratory and field test program. The main purpose of the laboratory work was to verify that these requirements on the TV picture-element (pixel) level can be satisfied with currently used vidicons, while the main purpose of the field work was to determine comet detectability.

PRECEDING PAGE BLANK NOT FILMED

SECTION III  
TEST DESCRIPTION

A. VIDICON TEST SET

The purpose of the vidicon test set was to flexibly emulate the Mariner 2.54-cm (1 in.) flight cameras to supplement flight optical guidance demonstration data with laboratory and observatory optical inputs and to explore the accuracy of limiting vidicon parameters in a stable and repeatable manner.

The test set consisted of a camera head and its rack mounted support equipment, including the camera controller, recorder interface and control, digital tape recorder, slow scan monitor, and power supplies. The test set was designed to accommodate three optical inputs: a standard Optoliner for bench checkout; the scene simulator for laboratory star-target body tests; 20-cm aperture, 2-M focal length telescope for field tests.

The sensor selected for test was a GEC tetrode vidicon, model 1306-062, with characteristics as follows:

- (1) Size, 2.54 cm (1 in.).
- (2) Target type, storage (selenium sulfur).
- (3) Reseaux, MVM science camera pattern.
- (4) Deflection and focus, magnetic.
- (5) Mesh, separate.
- (6) Filament, 6.3 V, 100 mA with black painted envelope base.

Although the electron optics of the vidicon differ from the GEC flight triodes, the operating parameters were set up to maximize the similarity of performance. The deflection and focus assembly was of the same type as the flight units, a Celco model WV129, with a 5.0-mH horizontal coil, a 25.0-mH vertical coil, and a 50 mA focus coil. The sweep circuits used were the Mariner-type of analog for horizontal, and high-resolution digital for vertical. The vidicon format was square. A 500 line by 500 pixel format was used for preliminary tests, and a format of 800 lines by 800 pixels was used for the final laboratory tests. The horizontal retrace time (not included in the active format) was a fixed 50 elements. The frame readout times for the 2 formats were 15s and 35s, respectively.

The video chain consisted of a baseband, current-mode preamplifier with line clamping, integrate and dump pixel filtering, and 12-bit analog-to-digital conversion. The resulting video peak signal-to-noise ratio was 220 to 1 in the horizontal direction, and 170 to 1 in the vertical direction. The lower vertical number was due to residual quantization noise in the vertical sweep.

Vidicon performance parameters that were measured as a background to the guidance tests were dark current, filament exposure, erase factor, image storage, exposure reciprocity, and star transfer. Data for the first three were taken at the format of 800 lines by 800 pixels, while the remainder were taken at 500 lines by 500 pixels.

Dark current build-up, filament exposure, and erase factor were measured with the read target voltage at 11.0 V, the erase target voltage at 11.5 V, beam current at 2  $\mu$ A, and filament voltage at 5.5 V. The time for the dark current to reach 35% of the full scale video signal (with the filament "off") was measured at 165 min. A dark current increase of 30% was measured with continuous filament exposure. The erase factor<sup>2</sup> was measured at 40% for the first three residual reads, falling to 25% on the seventh read.

The test of total net-star image storage resulted in a 93% signal recovery after 21 min. Exposure reciprocity measurements indicated a 25% loss in net star sensitivity for a 25-min. exposure. The camera's star transfer curve was measured for five different brightness stars (Fig. 1). The mid-range gamma was 1.05, dropping to 0.77 near full scale exposure and rising to 1.5 at the lowest detectable levels.

#### B. TEST SET OPERATIONS

The test controls were designed to permit operation in either a fully automatic mode, or to use any of the various cycles independently of the others. As an example, different amounts of background signal were generated by initiating the erase cycle with flooding, stopping the cycle before erase, reading the vidicon a predetermined number of cycles to achieve the desired background level, exposing, then writing the data on the tape recorder. A complete list of test set operational controls is provided in Appendix A.

<sup>2</sup> Percent of net signal remaining after one normal vidicon read.

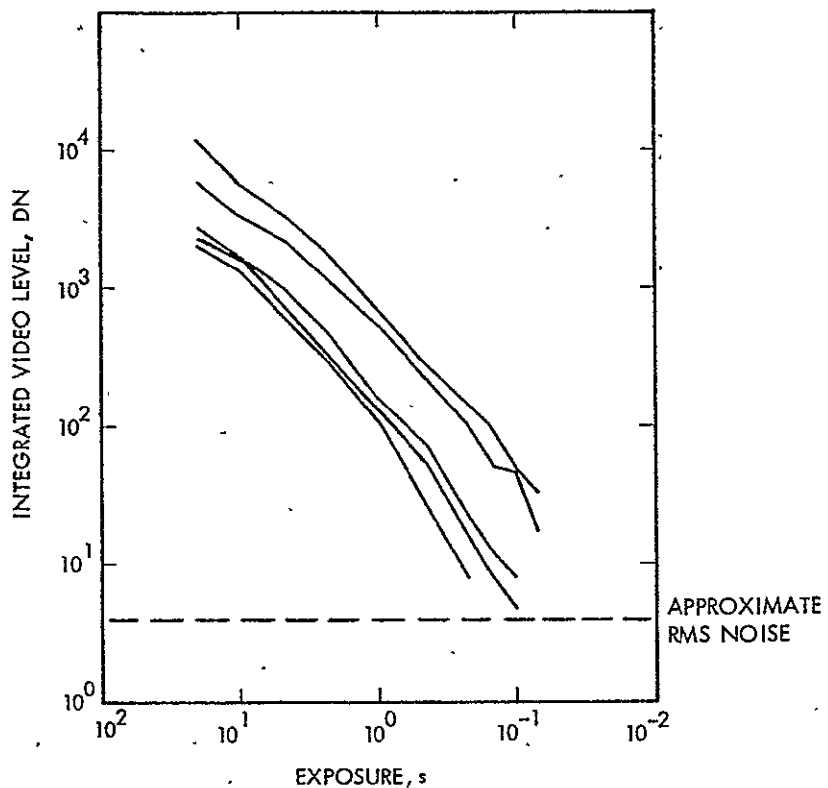


Fig. 1. Star Transfer Characteristics for Laboratory Simulated Star Images

#### C. TEST SET BLOCK DIAGRAM

A block diagram of test camera head is shown in Fig. 2. The philosophy of the camera design was to make the camera head as self-contained as possible with the ability to float ( $\pm 1$  V) relative to the controller electronics. Isolation was enhanced by the use of an RF filter connector to reject interfering pickup in the connecting cable. Examining the individual blocks, the tetrode vidicon was operated at anode potentials that were set as high as practical to maximize resolution. The feedback shunt regulator provided the following voltages for the laboratory tests:

G4 (mesh)	1010 V
G3	801 V
G2	300 V

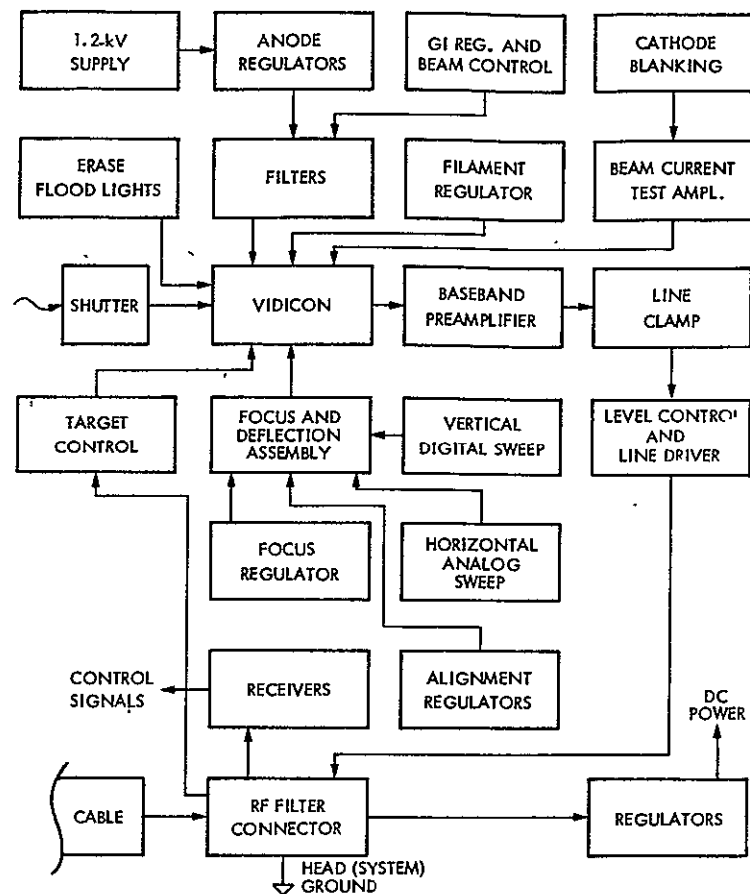


Fig. 2. Optical Guidance Data Laboratory (OGDL) Test Camera Head Block Diagram

The transconductance preamplifier used an  $80\text{-M}\Omega$  feedback resistor. The resulting 15-kHz bandwidth more than adequately passed the 10-kHz video. Sufficient post amplification was used to raise the full scale video level to 5 V for transmission to the controller electronics. The preamplifier input noise was measured at 1.5 pA with a 7.5-kHz bandwidth.

A conventional, flight type of analog integrator and current feedback horizontal sweep was used. However, the vertical sweep was generated with a 16-bit, monotonic digital-to-analog converter with a current feedback driver.

The separate camera controller/recorder block diagram is shown in Fig. 3. The heart of the controller was a crystal oscillator-driven, 32-stage counter/clock chain. All timing was derived from it. The fundamental period of the test set was the fixed pixel period of 50  $\mu$ s. This period was determined by the packing density of the tape recorder and operation at its maximum, continuous recording speed. Synchronization of the tape recorder, including gap generation, was assured by generating all control signals externally from the master clock.

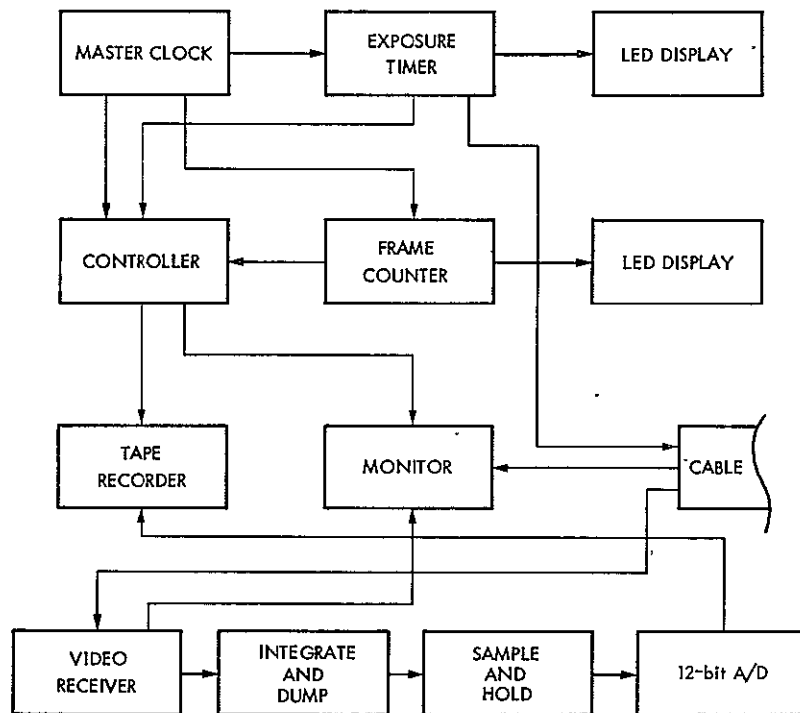


Fig. 3. OGDL Test Camera Controller/Recorder Block Diagram

The monitor was a highly modified Conrac 36-cm (14 in.) unit. Modifications included conversion from triggered to DC coupled sweeps and new beam blanking.

The first block of the controller video chain was a receiver made of RF prefilters and a commercial instrumentation amplifier. This receiver effectively rejected head ground offsets and cable pickup. The next stage was a pixel-timed integrate-and-dump video filter, which determined the

video filter noise bandwidth. Following that, a sample-and-hold circuit fed a 12-bit analog-to-digital converter, which processed the signal for the tape-recorder. The tape recorder was an 1108 compatible, seven-track machine. Video was recorded in two, sequential, six-bit bytes.

#### D. LABORATORY DESCRIPTION

The laboratory was built as a dedicated facility with close temperature control of  $\pm 1^{\circ}\text{C}$  for mechanical and optical stability. The scene simulator was mounted on a 1.2 by 2.4-m seismologically isolated and self-leveling granite slab and was covered by a filtered laminar-flow hood used to keep the optics clean. The simulator is shown in Fig. 4 and, in schematic form, Fig. 5. It consists of two projectors with superimposed images, one for the star field and a second, independently controlled, for the target image.

The star projector used a zoom illuminator lens to uniformly illuminate the backside of a star mounting plate. The zoom lens permitted illumination control over a range of 250:1. The star plate was precision bored with an orthogonal matrix of 64 holes on 2.54 cm (1-in.) centers. Each hole could be fitted with one star plus one neutral density filter, or with an opaque plug. The simulated stars were produced by small sapphire spheres. Star intensity was a function of the sphere diameter. Each sphere behaved as a small condenser lens producing a small ( $<2\mu\text{m}$ ) geometric image, much brighter than a pinhole of the same size. Further relative intensity control was possible through the use of individual plug-in neutral density filters in a range of neutral density (N.D.) 0.1 to 1.0.

The target body illumination was similar to that of the star projector, except that a wedge-filter intensity control was used with a fixed focal length illuminator lens. The wedge filter provided an intensity control range of  $10^5$  to 1. The target body slide was mounted on a condenser lens, where the image was in focus, and the magnification was 12:1. An alternative location was between the wedge filter and illuminator lens at a magnification of 1:1. Test slides were prepared for use here but were rejected because of poorer optical quality.

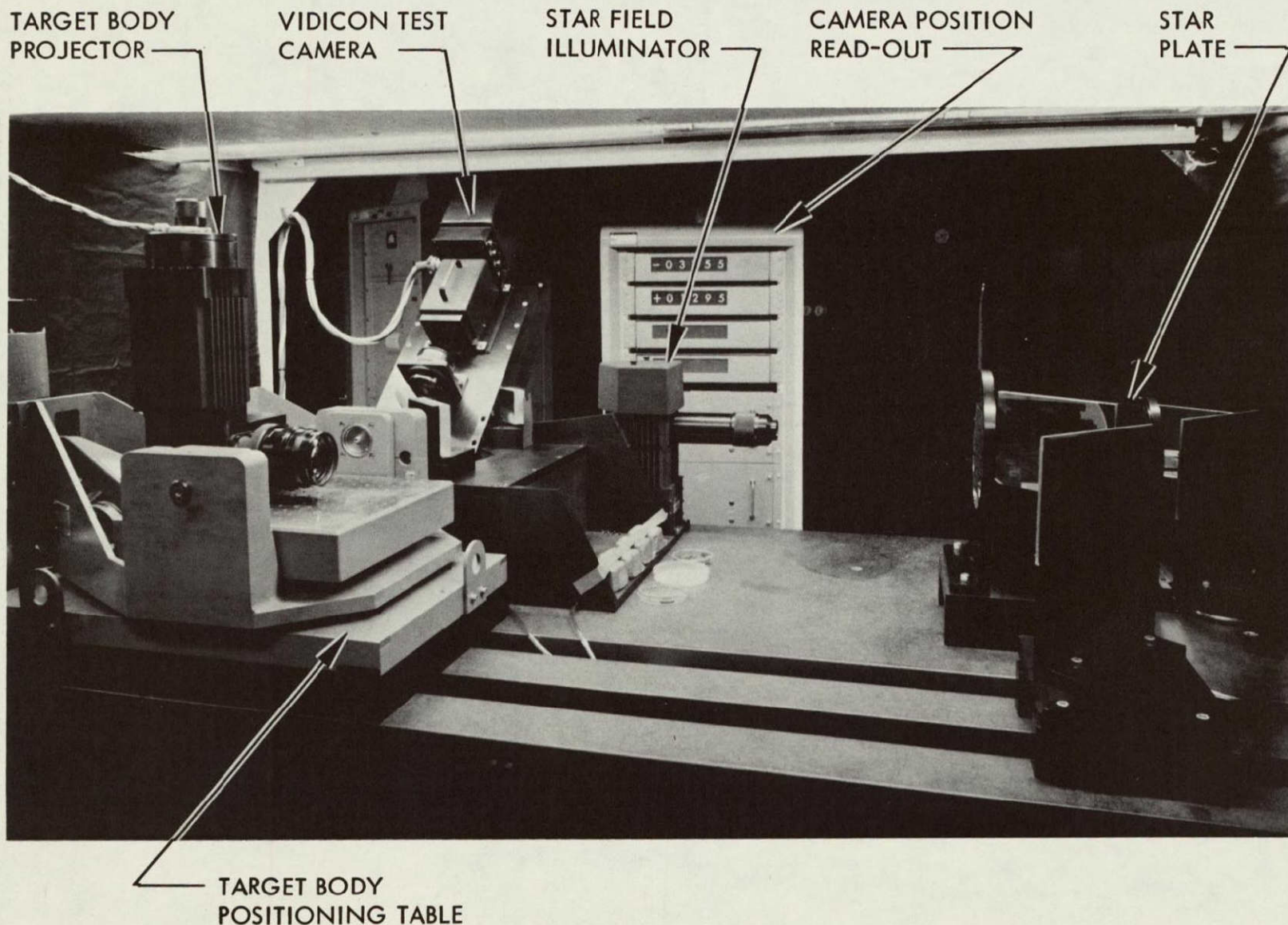


Fig. 4. Laboratory Set-Up Optical Scene Simulator With Selenium Vidicon Camera

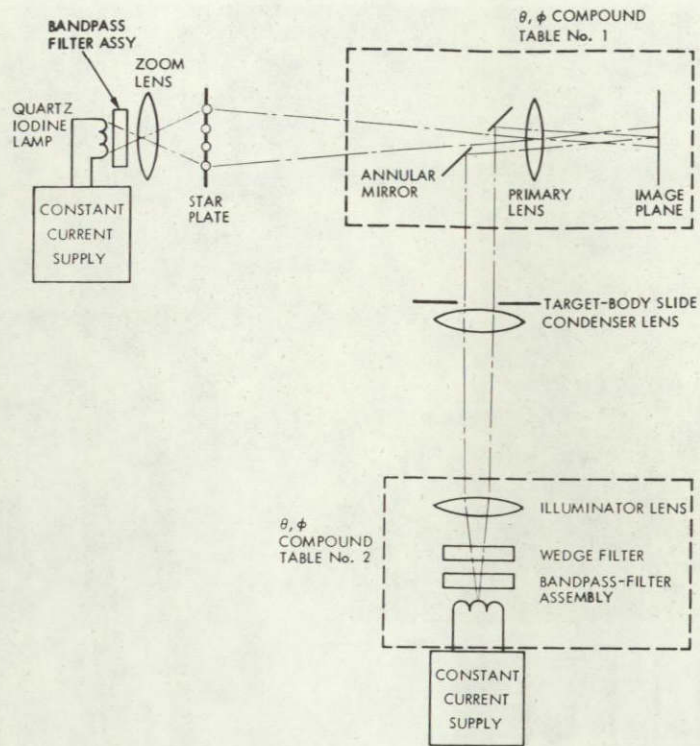


Fig. 5. Scene Simulator Configuration

A 45-deg annular mirror was located in front of the primary lens such that the stars were imaged through the hole and the target bodies were imaged by reflection from an elipsoidal annulus around the hole. The primary lens was a 135-mm focal length of f/2.0 Zero Nikkor stopped down to f/2.5. The optical bandpass filters were selected to give the minimum of chromatic aberration with a resulting passband of 480-500 nm. The star image point spread was about 5 to 6  $\mu\text{m}$  to the first minima and that of the target body was about twice as large.

#### E. SCENE SIMULATOR CALIBRATION EQUIPMENT AND DESCRIPTION

Since the basis of the operation of the vidicon characterization system was to compare the video-signal-derived star and target body positions to the actual (optical) locations, equipment to make direct position (and intensity) optical measurements was required and was developed for the purpose. This equipment is shown in schematic form in Fig. 6. It was

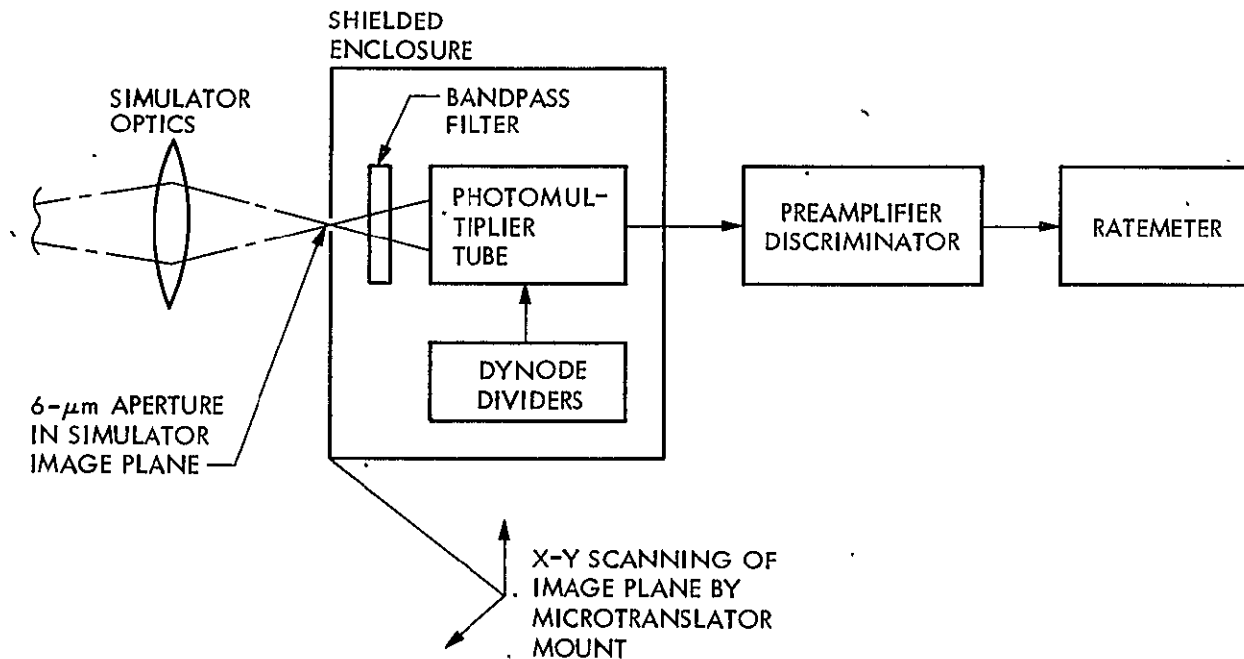


Fig. 6. Scene Simulator Calibration Equipment

positioned in the focal plane of the simulator in place of the vidicon camera head and consisted of a photomultiplier tube in a shielded enclosure with an interchangeable scanning aperture, an optical filter, and dynode dividers. This assembly was mounted on an XYZ microtranslator to form the complete calibration equipment assembly. The scanning aperture was positioned to be in focus on the simulator image.

Apertures from 250  $\mu\text{m}$  to 6  $\mu\text{m}$  in diameter were available. The larger apertures were useful for radiometric measurements, whereas the smallest one was used for position and image profile measurements. The apertures were each radiometrically calibrated by substitution. The optical filter matched the transmission characteristics of the two illuminators and thereby greatly reduced sensitivity to any unwanted white stray light.

The X and Y positioning microtranslators read directly to 1  $\mu\text{m}$ , with a motion range in excess of twice the vidicon image size. The Z-axis translator was used only for focusing. The depth of field was about 20  $\mu\text{m}$  with the 6- $\mu\text{m}$  aperture.

The photomultiplier tube was operated in the photon counting mode for maximum sensitivity. The photon counting chain used a preamplifier-discriminator in close proximity to the PMT, which was powered by a ratemeter type of indicator. An 8- $\mu\text{m}$ , S-11 photocathode was selected to minimize the uncooled dark count rate (18 counts/s) and to maximize the quantum efficiency (12%) at the wavelength of interest.

#### F. VIDEO DATA PROCESSING

The video data processing and parameter estimation was performed using two programs from the optical navigation program set developed for the Viking mission to Mars (Ref. 6). The conversion from the spacecraft-oriented coordinate systems to the laboratory set-up was relatively simple, since these programs were written in a manner to facilitate changes for future missions. How this conversion was achieved and how these programs were used will be discussed below.

## 1. Optical Data Calibration and Rectification (ODCR) Program

This program was designed to calibrate spacecraft parameters by comparing star- and satellite-image locations found in the video data with the known locations derived from star catalogs and target ephemerides. Thus, to be of use for the laboratory, it was necessary to define a set of "pseudo-spacecraft" coordinates that would correspond to the laboratory set. The selected configuration is shown in Fig. 7 and provides the following correspondences:

- R coordinate of starplate  $\leftrightarrow$  Star right ascension
- T coordinate of starplate  $\leftrightarrow$  Star declination
- Compound table azimuth  $\leftrightarrow$  Spacecraft roll
- Compound table elevation  $\leftrightarrow$  Spacecraft yaw
- Inclination of reflected optical axis  $\leftrightarrow$  Spacecraft pitch

To achieve this configuration, the following ODCR input parameters were used:

- (a) Clock angle of X axis = 0 deg.
- (b) Reference star right ascension/declination =  $0^\circ$ ,  $0^\circ$ .
- (c) Sun vector in X, Y, Z = (0, 0, 1).
- (d) Platform clock angle = ( $0^\circ$ ).
- (e) Platform cone angle = ( $90^\circ$ ).

Since the star plate is flat and the right ascension/declination are spherical coordinates, it is necessary that the right ascension/declination remain small to minimize the nonlinearities. Therefore, a convenient scale factor of 0.039 deg/cm (0.1 deg/in.) was introduced. With this scaling, the maximum nonlinearity effect at the edge of the 22-cm illuminated area is:

$$11M [1 - \cos (0.039 \times 11)] \approx 0.3 \mu\text{m}$$

where

$$M = \text{Optical System Magnification} = 0.0873665$$

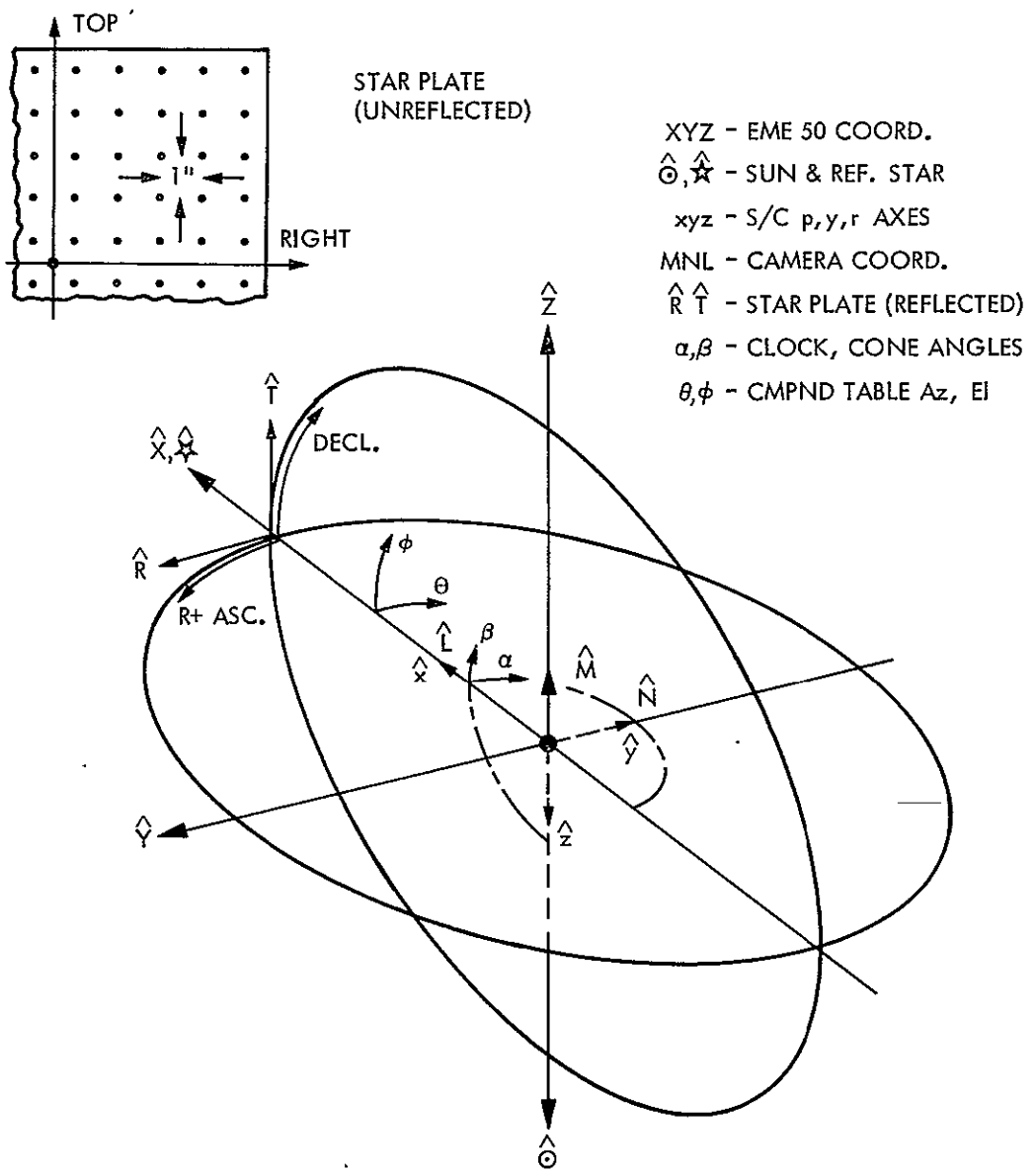


Fig. 7. Pseudo Spacecraft Coordinates

The focal length was then selected so that a star in ODCR (right ascension/declination) maps into the same image plane location as the corresponding star in R-T coordinates. To do this, an a priori value for the focal length of 1.27146 meters was input to ODCR. Then the focal length parameter was estimated using a Kalman filter in ODCR so that the mapping residuals between star locations was minimized. The focal length was estimated for each picture separately, and each fell within 0.05% of the a priori value.

## 2. Image Processing Program (IMP)

This program extracts image locations from the digitized video data which reside on magnetic tape. The first problem with using this program was to convert the raw video data to a form acceptable by this program. To do this, the least 4 significant bits (out of a total of 12) of each pixel had to be deleted. This loss of data did not affect the measurement accuracy because of the smoothing and approximation algorithms within IMP. Other than the loss of four bits per pixel, the video data was unchanged (e.g., no noise reduction).

The locations of stars and reseaux were found by extracting small regions surrounding those images and examining them manually. To locate the target center, each line in an area containing the target image was scanned by computer until two pixels in a row were found to be above a pre-determined threshold parameter. A limb point was then determined for that line by interpolating to the exact threshold level. Once all the lines were scanned and the limb points determined (~150 points), an ellipse of constrained shape and size was fitted to those points in the least square sense. The center of that ellipse was then taken as the target image center. Unconstrained ellipses gave very nearly the same locations (<1/4 pixel ~3  $\mu$ m) whereas slight changes in the camera parameters, e.g., focal length, gave the same results to the measurement accuracy presented.

In an attempt to determine how the selection of a threshold for limb-point definition affected the center location, three thresholds were used. Because the intensity level varied greatly from picture to picture, it was necessary to set up an algorithm for determining each threshold so that they would correspond with the similar threshold from any other picture.

The first threshold (Fig. 8, Level I) used was selected just above the background level. This threshold was only used on a limited but representative selection of the pictures. It was found that this low level threshold yields center locations which differ greatly depending on intensity level. This effect is due to image flare and blooming. The second threshold level (II in Fig. 8) was defined as the midpoint between background and target intensity levels. The last threshold (Level III) was selected at a point just before the rising intensity level begins to smooth out into the target. These thresholds correspond roughly to 10%, 60%, and 85%, respectively, of the peak image intensity level.

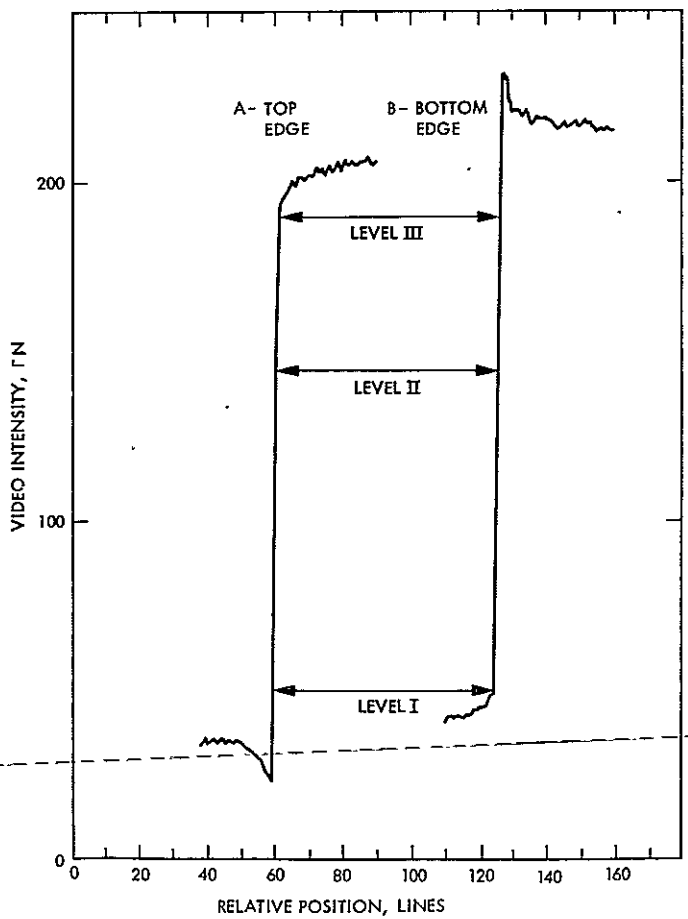


Fig. 8. Typical Disk Limb Profiles (Range of contour levels used for center-findings shown)

### 3. Image Plane Measurements

As explained above, a microradiometer was used to measure the star and target locations in the image plane. The star location was found by scanning the star image to find that point at which the photon count reached a maximum. That point was taken as the first approximation to the star-image center. Horizontal and vertical scan through that point were then made, noting the photoncount versus scan distance. This process allowed a profile of the star image to be made from which a more accurate image center could easily be obtained.

To obtain the target location in the image plane, several horizontal and vertical scans were made completely through the target image. When the photoncount reached a level of 2%, 50%, or 75% of the count inside the image, a limb point was defined. Thus, each scan yielded three pairs of limb points. The IMP program was then used to fit a circle to each set of limb points.

The star and target locations in the image plane were then mapped back to the star plate coordinates by the following transformation:

$$\begin{matrix} R \\ T \end{matrix} = \frac{1}{M} \begin{pmatrix} \cos \theta & \sin \theta \\ -\sin \theta & \cos \theta \end{pmatrix} \begin{pmatrix} \Delta X \\ \Delta Y \end{pmatrix}$$

where

$\Delta X, \Delta Y$  = offset of star location from the center star and

$\theta = 45$  deg

M = optical system magnification

### 4. Vidicon Calibration Using Reseaux

Calibration of the vidicon center, linear transformation to image plane, and electromagnetic distortion were done using measured reseaux location on the face of the vidicon and reseaux image locations from an initial test frame.

## 5. Data Flow

The sequence of events (Fig. 9) for one picture-taking sequence began with calibrating the microradiometer and obtaining the image plane measurements. Next, a high degree polynomial was fit to the microradiometer calibration data by computer, and the corrected image plane measurements were obtained using IMP (as described in Section IV). Also, the video tape was preprocessed to obtain a data tape compatible to the IMP program.

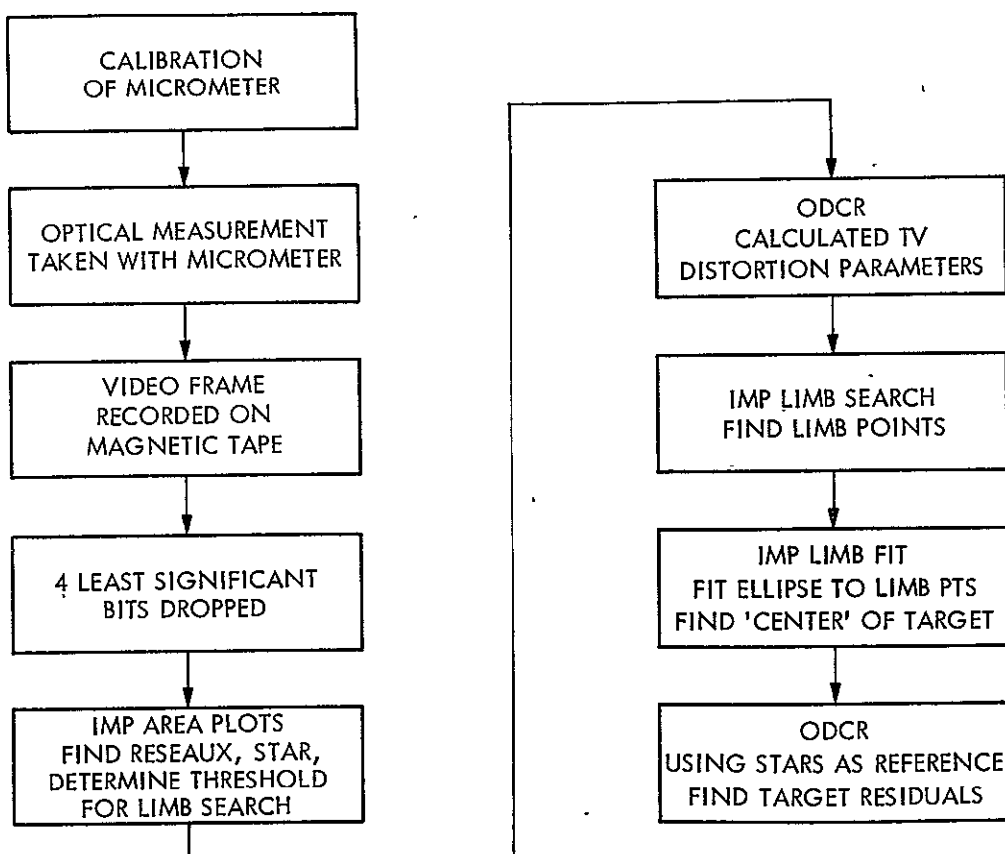


Fig. 9. Laboratory Measurement Data Flow

Once the video tape was preprocessed, IMP was used to extract star and reseaux images and to determine the proper threshold for searching for the limb. The reseaux locations were then input to ODCR to calibrate the vidicon center and electromagnetic distortion. Next IMP was used to find the limb point of the target image and calculate the target image. Finally, the star-target image locations were input to ODCR where image location residuals were obtained by calibration of the camera focal length.

## SECTION IV

### FIELD TESTS

A series of field tests was performed to photometrically calibrate the vidicon system on a variety of astronomical targets. These tests also provided optical guidance data for objects which could not be simulated in the laboratory. Test targets included the moon, stars, planets, and two comets (Appendix B). The results obtained, when corrected for atmosphere absorption and optical system parameters, indicate a good correspondence between the sensitivity of the test vidicon and that used on Mariner 10 (Ref. 4). This result strengthens the applicability of test-sensor results to flight instruments. Moreover, comet data acquired in the field provides a good basis for predicting how early a comet can be detected during an actual mission.

To minimize the adverse effects of atmospheric pollution and lights, all field data were taken at a remote site northeast of Palm Springs. The test equipment (Fig. 10) included (1) a laboratory vidicon and associated test set, (2) Celestron 20-cm (8-in.) Schmidt-Cassegrain optics, (3) a 41-cm (16-in.) Cassegrain guide telescope, and (4) a video tape recorder for storing the test frame in digital form. A special two-axis adjustable mounting plate was built to enable some adjustment of the test camera boresight with respect to the guide telescope. This adjustment was needed to guarantee that the object tracked by the guide telescope would also appear in the vidicon frame. All guiding was done manually for exposures of 10 s to 10 min. Shorter exposures were unguided.

#### A. PHOTOMETRIC CALIBRATION

A primary objective of the field tests was to calibrate the test vidicon, using stars of known brightness. Not only did this permit comparison with flight cameras, but it also provided a means for calibrating the laboratory simulator in terms of stellar magnitude.

An example of a bright star image is shown in Fig. 11. Actually, this image is of the double star Gamma Leonis, the two dots representing the calculated relative position of the component stars. When exposures were short (i.e., there were negligible tracking errors), star-image diameters were found

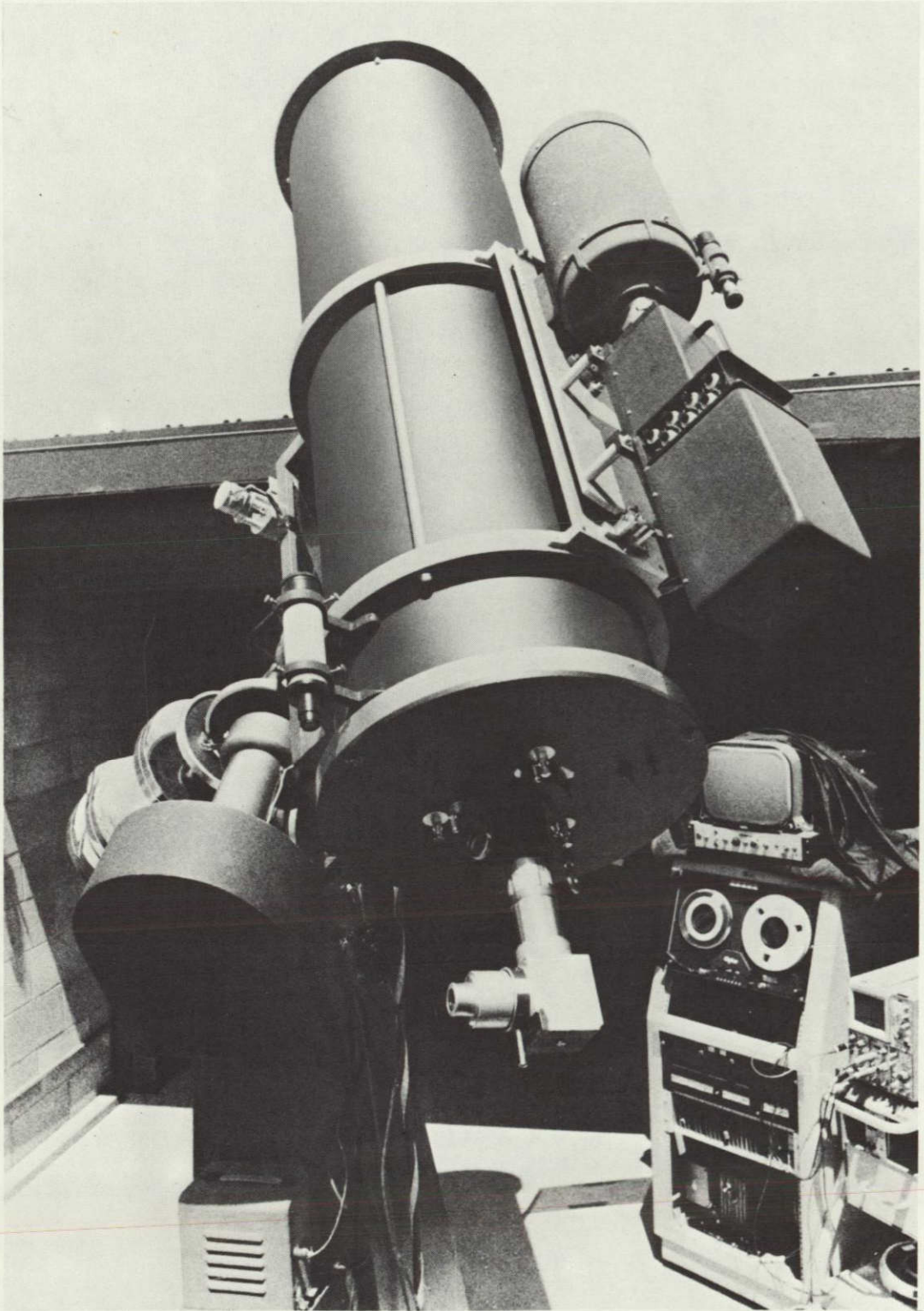


Fig. 10. Field Test Camera and Tracking Telescope

to be consistently 30 to 40% larger for the field test data compared to laboratory images. This increase is probably due to a combination of atmospheric "seeing" effects and imperfect focusing. Longer exposures often resulted in substantial further increase in image size because of guiding errors.

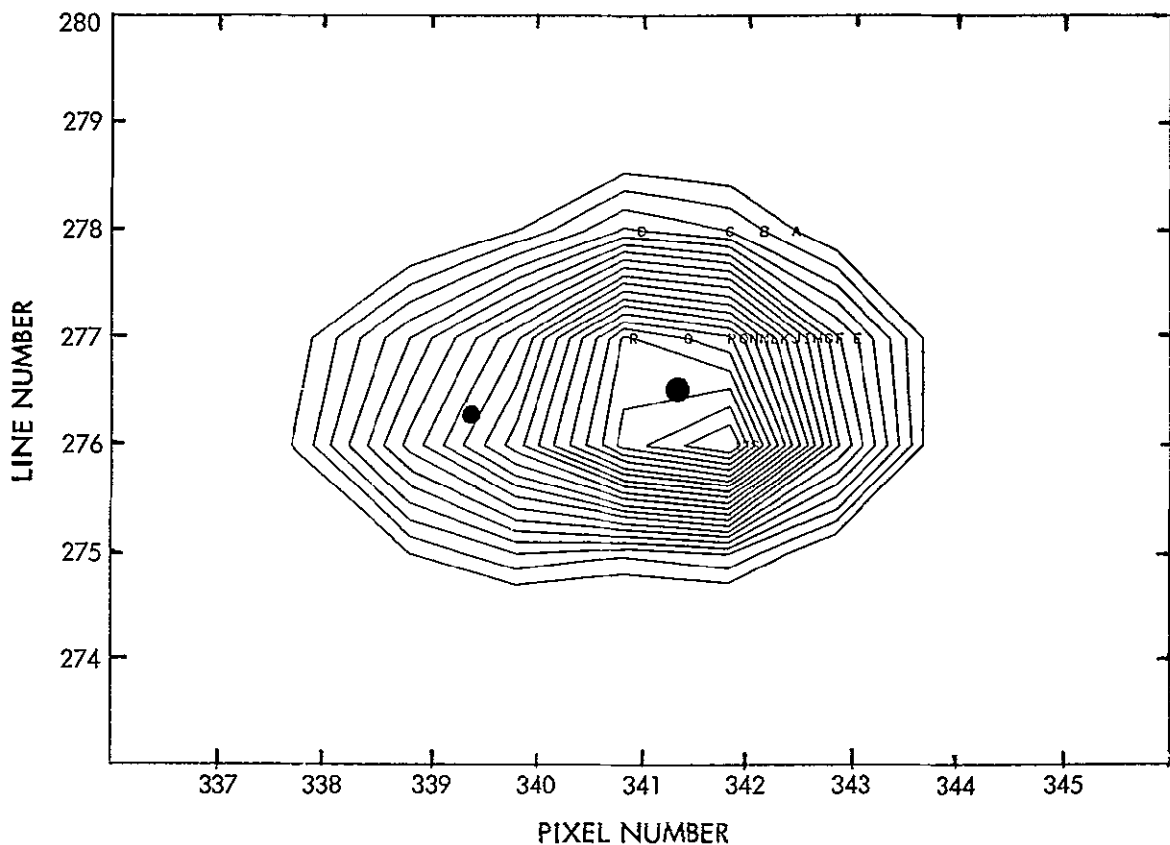


Fig. 11. Double Star Image from Field Test  
(Dots indicate predicted orientation)

Several factors must be included in analyzing the star data. First, the effects of variation of image size must be minimized. This minimization can be accomplished by measuring the integrated camera response (sum of signal minus background) over the entire star image, rather than a peak value. The integrated signal was found to exhibit fewer variations because of minor image smearing than peak signal and therefore provided a more consistent measure of camera performance.

A second factor is the importance of a star's spectral class on detection. Selenium vidicons are much more sensitive to near ultraviolet radiation (300 to 450 nm) than the human eye. As a result, blue stars (types O, B) will produce a relatively greater vidicon response than redder stars (G, K, M) of the same visual magnitude. The size of this effect has been calculated (Fig. 12) and applied as a correction to all field data.

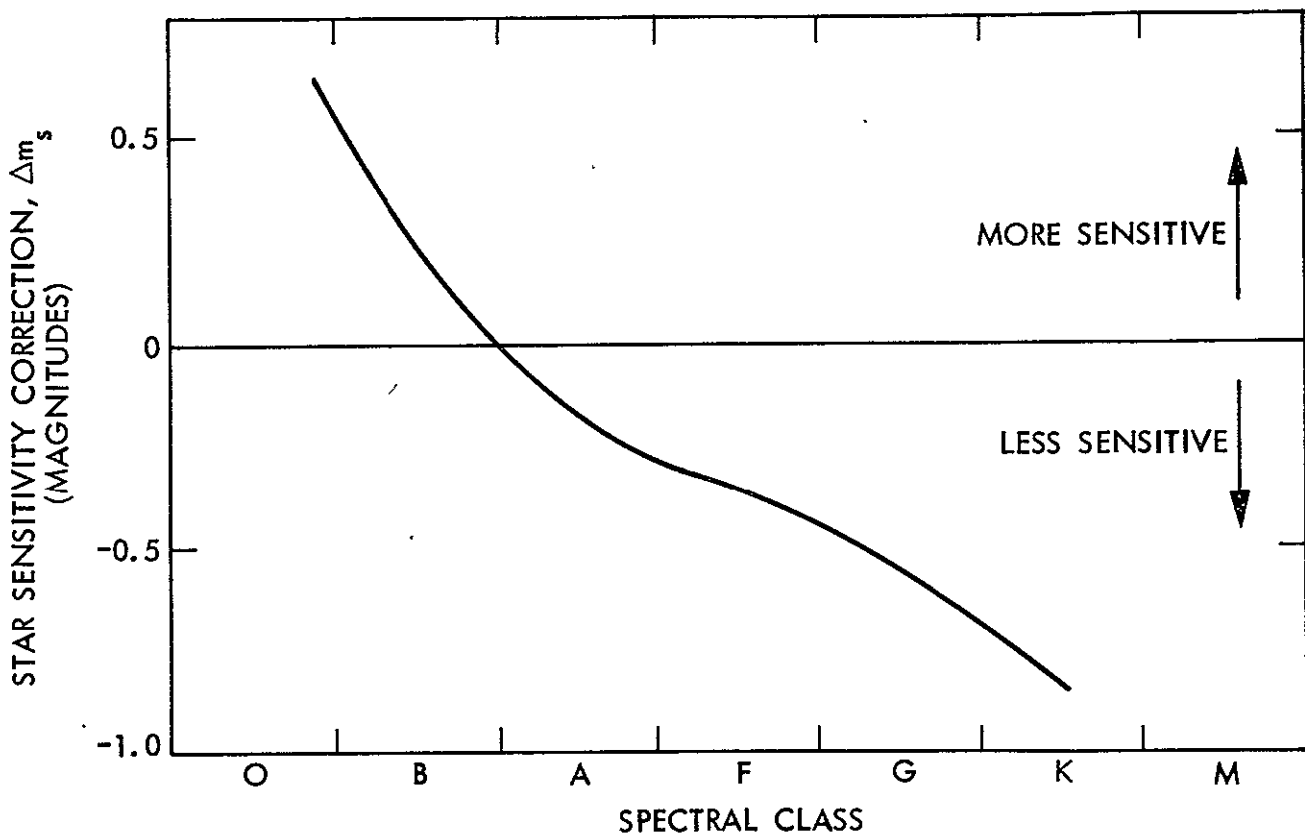


Fig. 12. Calculated Star Color Correction for Mariner Vidicons

Finally, a correction to allow for atmospheric extinction was made. For clear sky, the absorption is approximately

$$\Delta m = 0.22 \sec \theta$$

where  $\theta$  is the distance from the zenith of the object being viewed. Since the size of this correction was small, it was not necessary to include color factors.

Figure 13 presents star-sensitivity data after these corrections have been made and compares it to similar data taken on Mariner 10. The video signal was quantized to 8-bit resolution 256 grey levels or data numbers (DN) and summed over the entire star image. The average background was then subtracted and the result multiplied by a factor to take into account differences in optics and pixel size between the field camera and the Mariner 10 narrow-angle science cameras. The effective star magnitude was also corrected for exposure duration.

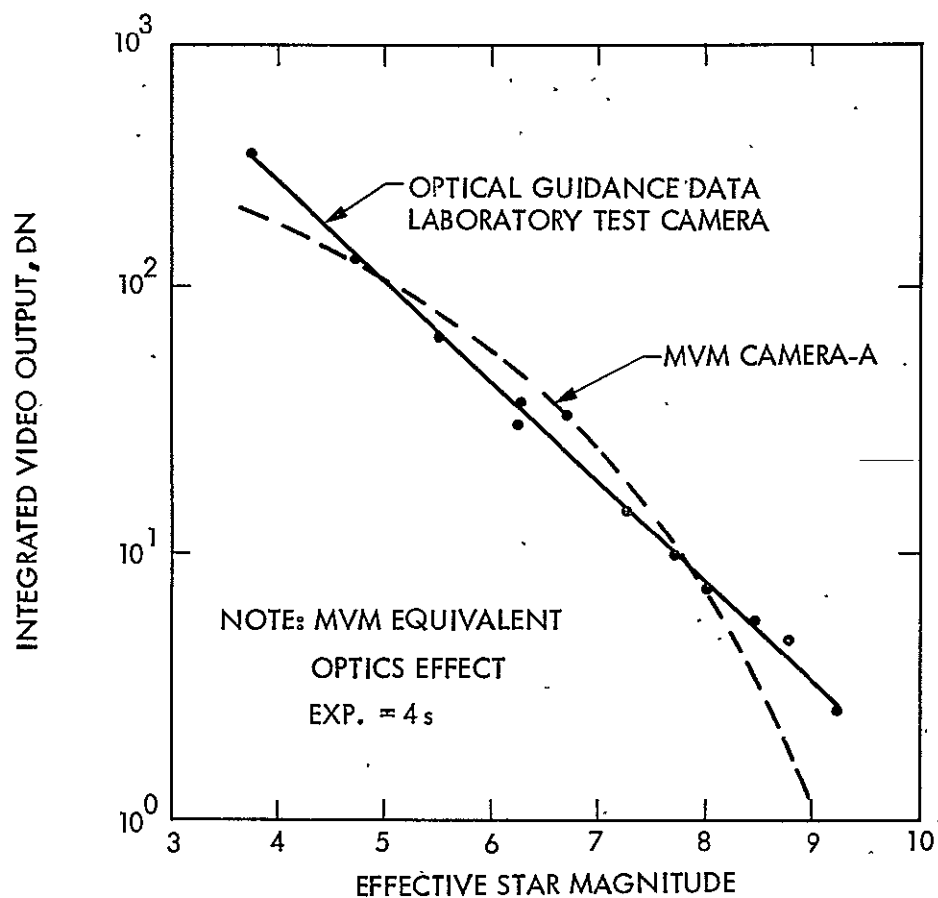


Fig. 13. Field Test Star Sensitivity of Test Camera (Effective star magnitude includes correction for spectral class, atmosphere, optics and actual exposure)

Several conclusions arise from the data in Fig. 13. First, the sensitivity of the two vidicons is very similar over most of the magnitude range. Although this may be fortuitous to some extent (individual vidicons can vary considerably), it does indicate that radiometric results derived in the lab should be applicable to current flight cameras.

Second, is the apparent linearity in test sensor response. This linearity is in contrast with Mariner 10 results (Ref. 4), wherein the sensitivity was observed to drop both for very bright and very faint (high magnitude) stars. The linearity of the test camera results, particularly those taken in the field, may be due to a combination of tracking error effects (causing blurring of star images) and higher background levels. Typical background levels for the test vidicon were running roughly 4% of full-scale,<sup>3</sup> well above Mariner 10 values. The linearity of the test camera response (as set up in the field tests) indicates that other photometric results, particularly the comet results in the following pages, were not influenced by variations in exposure duration.

#### B. COMET MEASUREMENTS

Future missions to comets will rely heavily on optical measurements for accurate navigation and science-instrument pointing. These measurements are required to compensate for the large ephemeris uncertainties present in the motion of most active comets, which would otherwise seriously degrade many scientific investigations. For this reason, it is important to quantify sensor performance so that accurate predictions can be made of how early the comet may be detected and how accurately its position may be measured.

Data acquired during the optical-guidance field test program has helped answer both of these concerns for the Mariner type of vidicons. Comet Bradfield, a condensed, moderately bright comet, was well placed for observation during field tests. Several data frames of this comet were obtained and analyzed. Fig. 14 shows one of these, a 10-min. exposure taken when the comet was approximately magnitude 7. The comet image is near the bottom of the frame, and the two streaks at the top are images of 8th magnitude stars, streaked out by motion of the comet during the 10-min. exposure.

---

<sup>3</sup> Intentionally set high for accurate reseaux location.

ORIGINAL PAGE IS  
OF POOR QUALITY

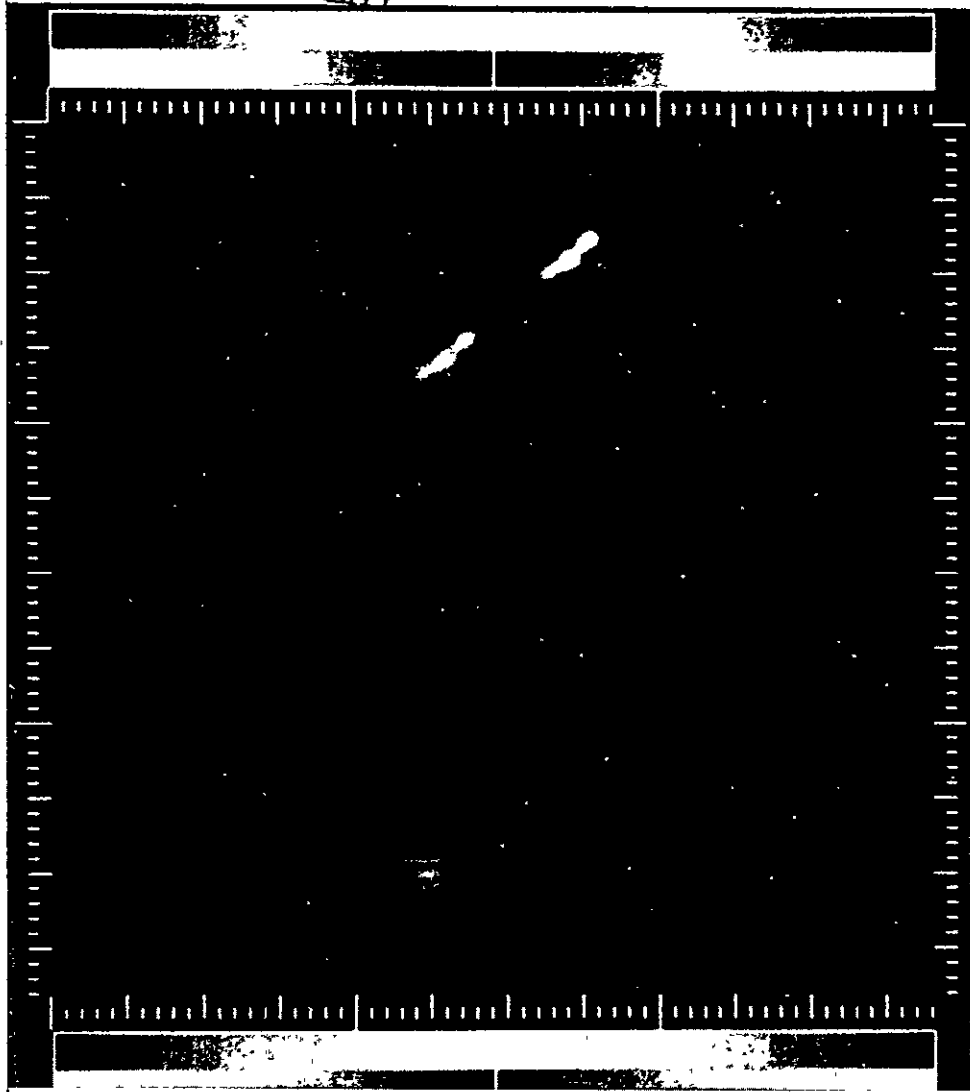


Fig. 14. Comet Bradfield Test Frame Exposure = 10 min.  
(Optics: 8" F.L., f/10)

One conclusion is apparent from even a cursory examination of Fig. 14. Even though the overall comet brightness was more than twice that of the 8th magnitude stars, its image is very much weaker. This is due to the diffuse character of comets and the fact that most of the light is emitted by the coma and tail, far from the nucleus. When the comet is imaged near the threshold of detectability, the diffuse light from the coma and tail is lost in sensor noise. Only the bright nuclear region is recorded. Thus, the visual

magnitude of a comet is not a direct indication of detectability. Once the visual magnitude of a star is corrected for spectral class, it can be used to accurately predict whether or not the star will be detected for a given set of exposure conditions. The same is not true for comets because of varying degrees of spatial compression and substantial differences in composition (ionic or dust tails, etc.).

Fig. 15 quantifies this conclusion for Comet Bradfield. Based on field-test data, the upper curve shows the exposure in seconds required to produce a threshold image of the comet with a narrow-angle science TV camera (Ref. 4). This curve is plotted against total comet magnitude including coma and tail. Also plotted are curves for comet detection versus nuclear magnitude, and star detection versus magnitude (derived from flight data and field tests). Note the difference of almost 4.5 magnitudes (60X) between detection of a comet and of a star of the same magnitude.

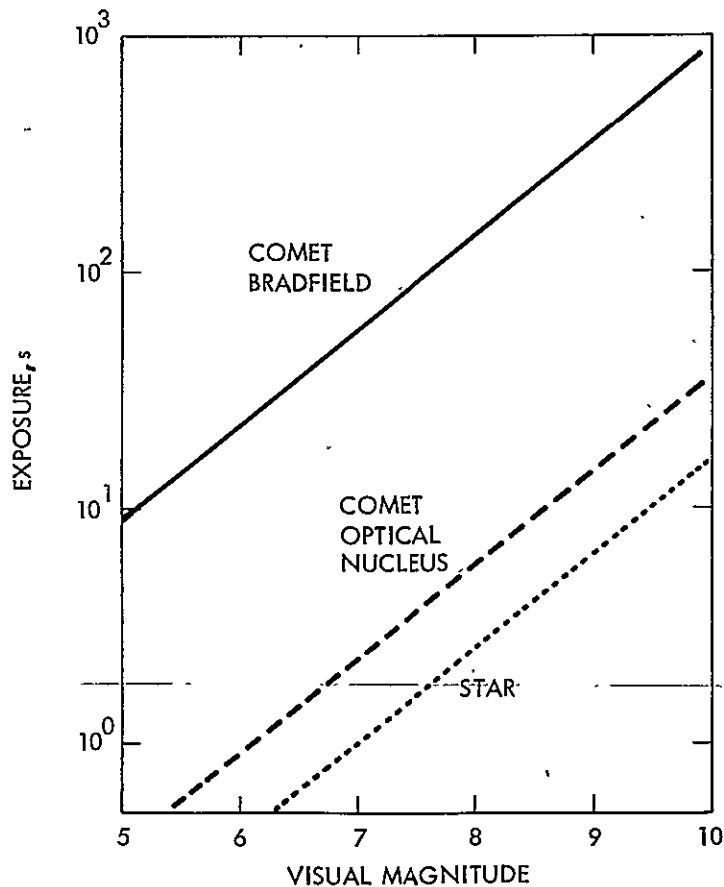


Fig. 15. Exposure Required for Detection  
(MVM Camera-Seconds)

Accurately finding the center of a comet video image raises problems not encountered in more conventional optical-navigation image processing. With a satellite/star scene, the star image is weak and covers only a few picture elements. Its center may be easily found by "eyeballing" contour plots of video intensity. The satellite image is a bright, extended target which presents a well-defined (if distorted) edge in the video data. Centerfinding for satellite images can be best accomplished using software which takes into account known distortions and a priori information such as image diameter.

The comet image, on the other hand, is both weak and extended, with no clear boundary for use by a centerfinding algorithm. A typical intensity contour plot is shown in Fig. 16. Some of the irregularities in this image (particularly the bright horizontal line) are pattern noise arising from imperfections (later minimized) in the line sweep circuitry (see Section II). However, most of the raggedness is caused by the low signal-to-noise level of the image.

The noise content of this image does not necessarily preclude accurate centerfinding, since the image spreads over many pixels. By averaging video intensity over several pixels the effective signal-to-noise level can be substantially increased. This is illustrated in Fig. 17 where a vertical slice is taken through the comet image and the average signal level from five adjacent pixels recorded. Even though the signal level is quite low (~2% of full-scale), the averaged video does not reflect the high noise content of individual pixel data (such as Fig. 16). This suggests that rather than finding the center of a particular brightness contour, an effective method of centerfinding for comet images would be to find the centroid of images slices such as in Fig. 17. Although this requires some modeling of the inner coma structure, the accuracy of this method should approach centerfinding accuracy for star images of similar peak intensity.

In conclusion, the field-test data point to three major findings for optical navigation on a comet mission. First, comet magnitude is not a good indicator of comet detectability since the diffuse nature of the comet illumination must be taken into account. Secondly, comet centerfinding, should be accurate to the pixel level or better even for images as weak as 1% of

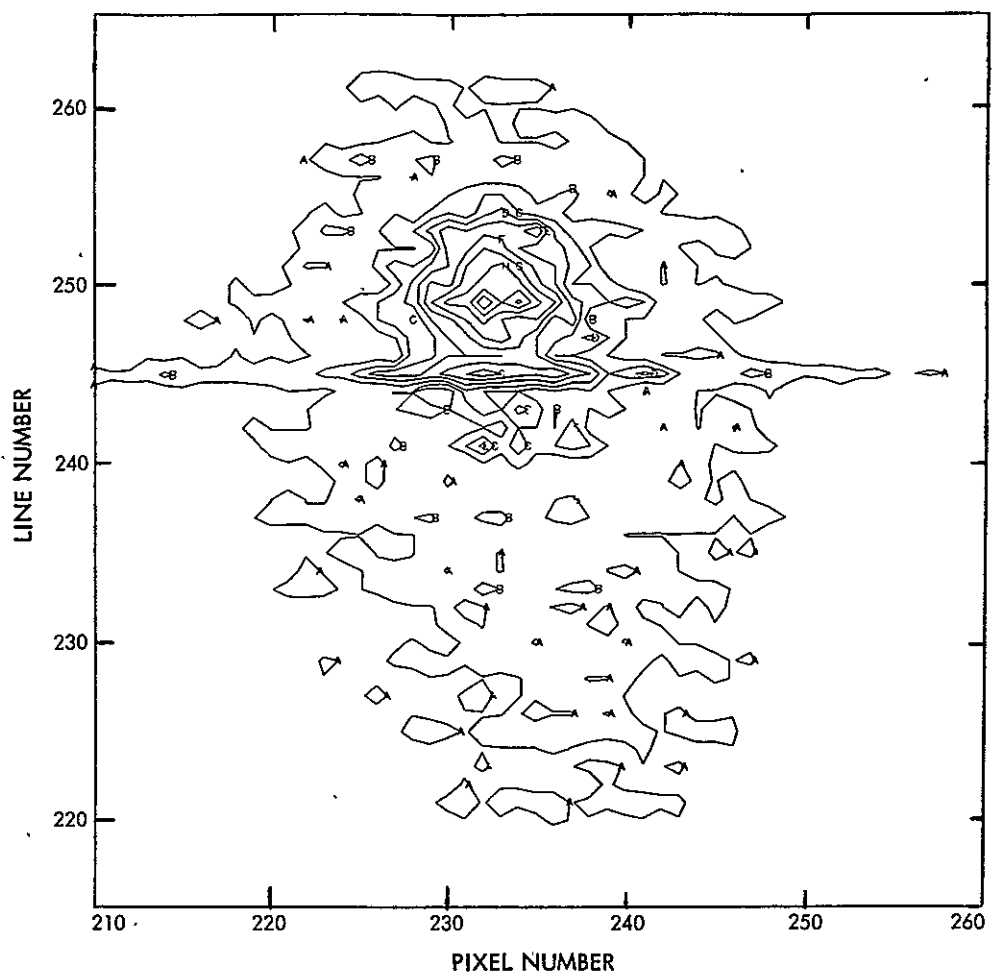


Fig. 16. Image Contour Plot—Comet Bradfield

full scale. Third, obtaining subpixel accuracy for weak images will require additional software development since neither star nor satellite centerfinding algorithms are appropriate.

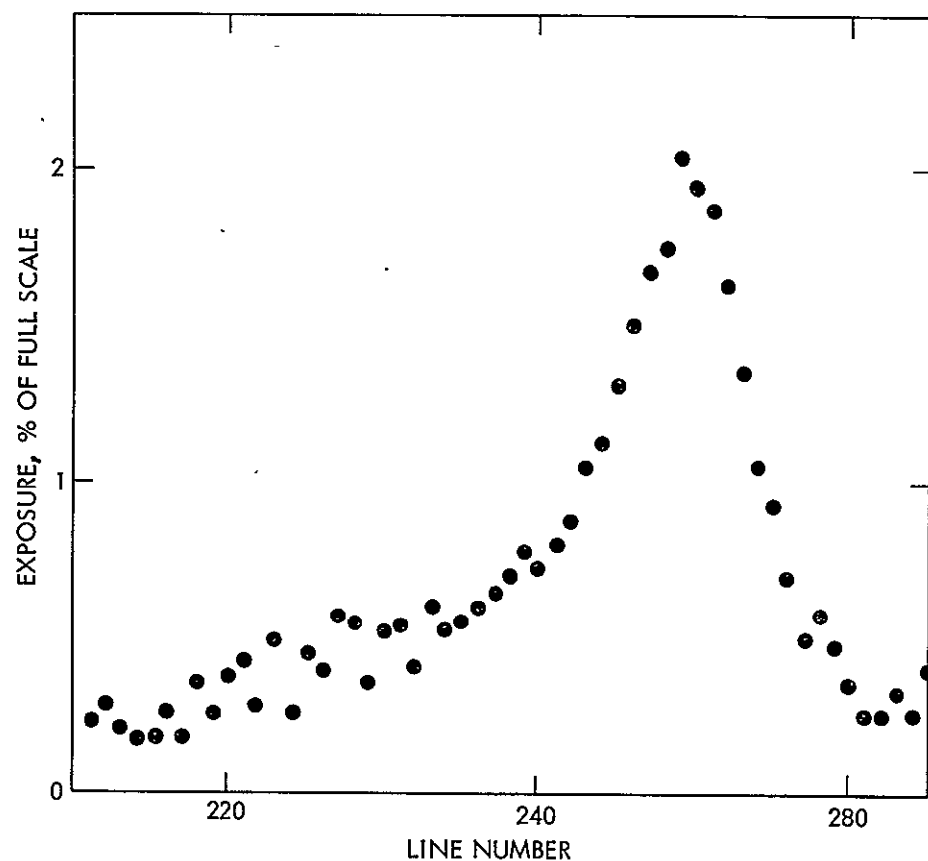


Fig. 17. Comet Bradfield Image (Five Pixel Ave.)

SECTION V  
LABORATORY TEST RESULTS

A. SIMULATOR IMAGE CALIBRATION ACCURACY

The accuracy of the measurement of the relative locations of star and target body images in the scene simulator was determined by the following error sources:

- (1) The microtranslator calibration accuracy.
- (2) The microtranslator repeatability.
- (3) The diameter of the scanning aperture.
- (4) The image-point spread characteristics.
- (5) Scene stability (position and irradiance).

The X and Y microtranslators were calibrated by transfer from an inspection reference-standard micrometer via dial gauges. The results are shown in Figs. 18 and 19. The data curves are the measured corrections to true readings. The X-axis, 7th order polynomial curve is the best least squares fit to the data. The deviation between the two is almost everywhere less than 1  $\mu\text{m}$ . The Y-axis correction curve is of 10th order, with a deviation of less than 2  $\mu\text{m}$  from the data. The polynomial fit correction-curves were used in position determination. The deviations reflect both error sources 1 and 2. The absolute contribution of source 1 alone is estimated at  $\pm 2.0 \mu\text{m}$ . A fairly thermostatic environment was required for the translator measurements since the calculated temperature coefficient was about 0.5  $\mu\text{m}$  per degree Celsius, a typical variation during the measurement sessions.

The first component of microtranslator repeatability errors was dial hysteresis, which was measured at  $\pm 0.5 \mu\text{m}$ . Other sources of hysteresis were in the translator carriages and inelastic flexure. These latter two were as large as 2-4  $\mu\text{m}$  but were minimized (to perhaps  $\pm 2.0 \mu\text{m}$ ) by always approaching the data points from the same directions.

The error introduced by the 6  $\mu\text{m}$  scanning aperture was less than the diameter and, in combination with the image-point spread characteristics, is estimated at 4  $\mu\text{m}$ . Measured image profiles are shown in Fig. 20 for a star, Fig. 21 for a clear disc, and Fig. 22 for a 30-deg phase disc.

Fig. 18. Calibration Equipment X-Axis Correction

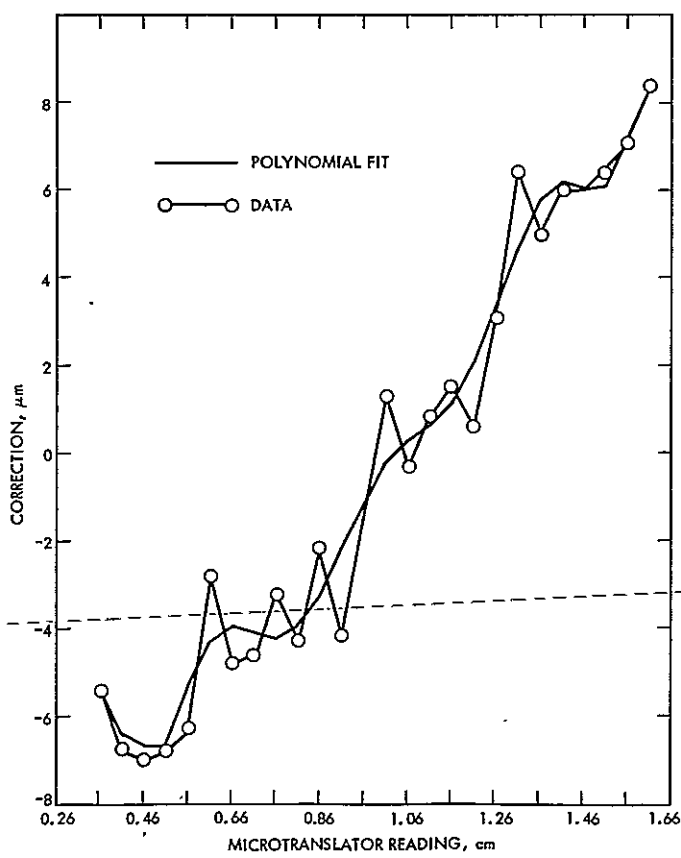
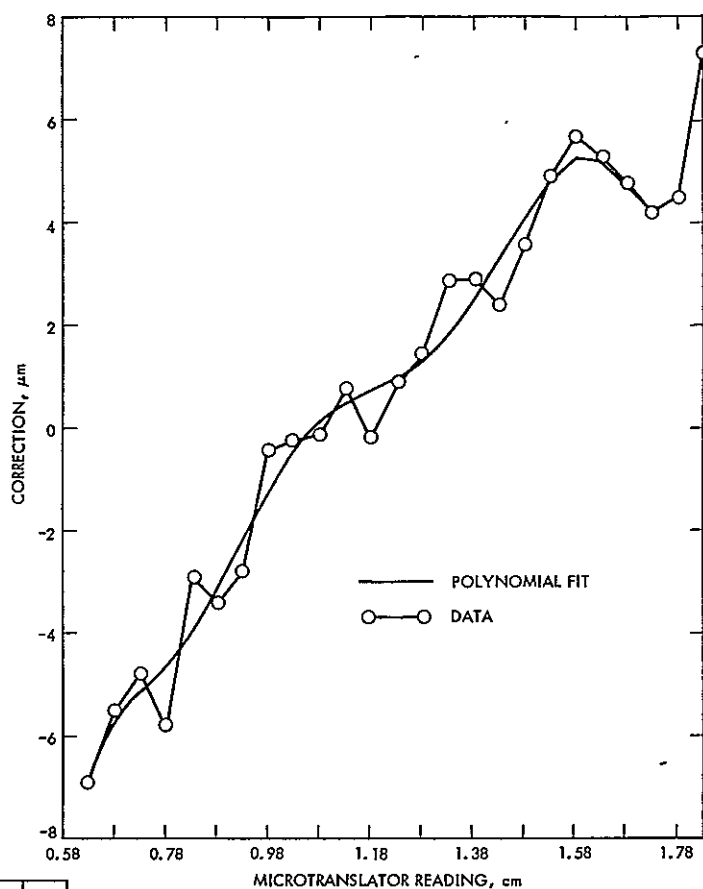


Fig. 19. Calibration Equipment Y-Axis Correction

Fig. 20. Center Star Top Profile

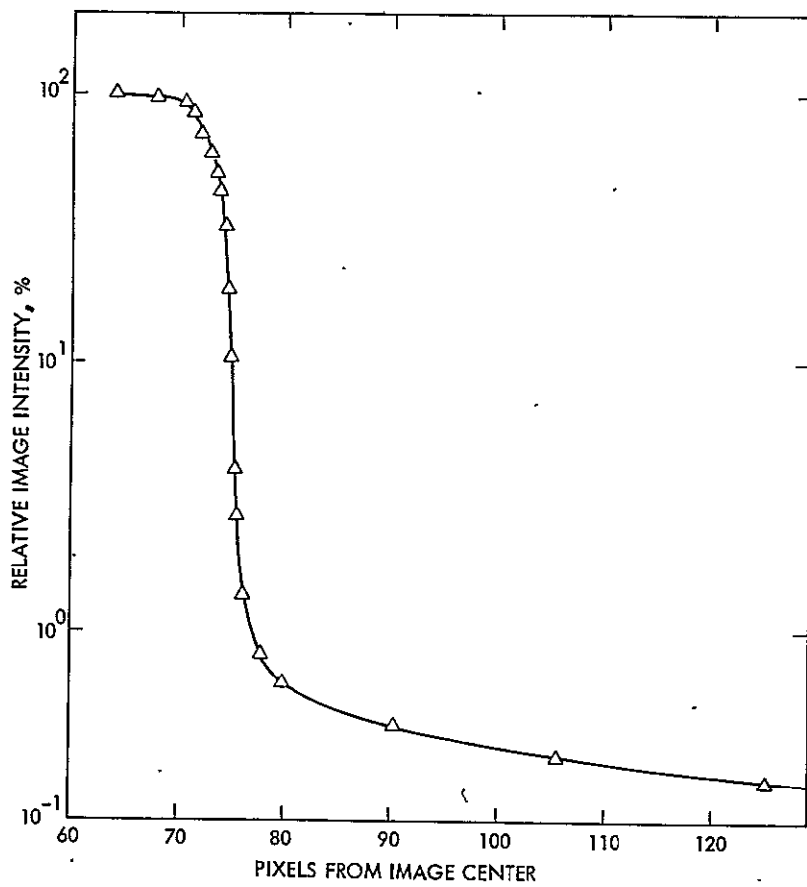
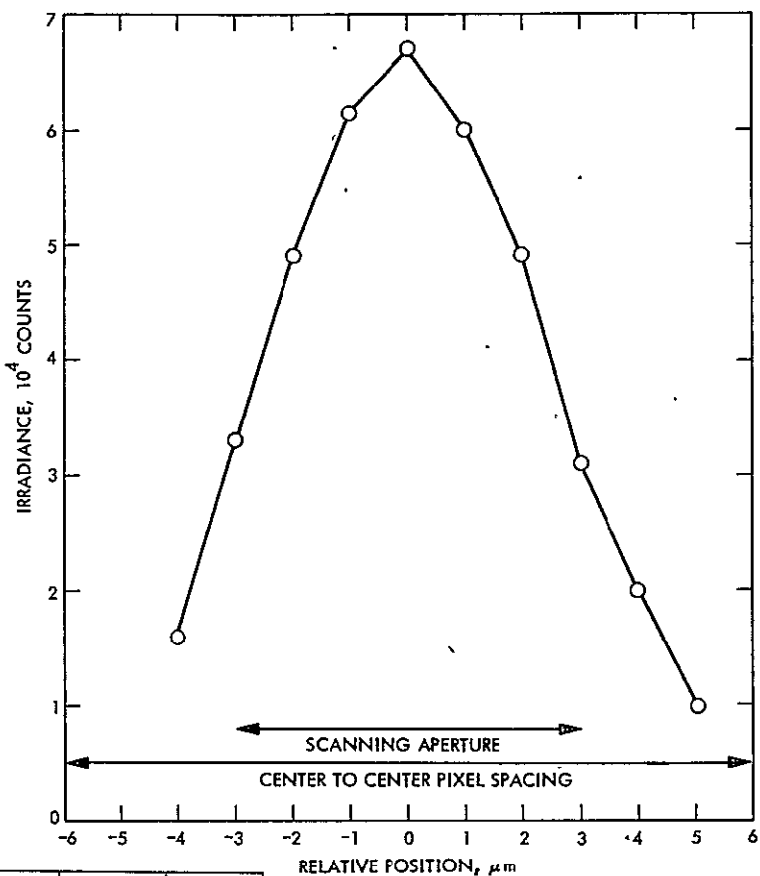


Fig. 21. Clear Disk Image - Edge Profile

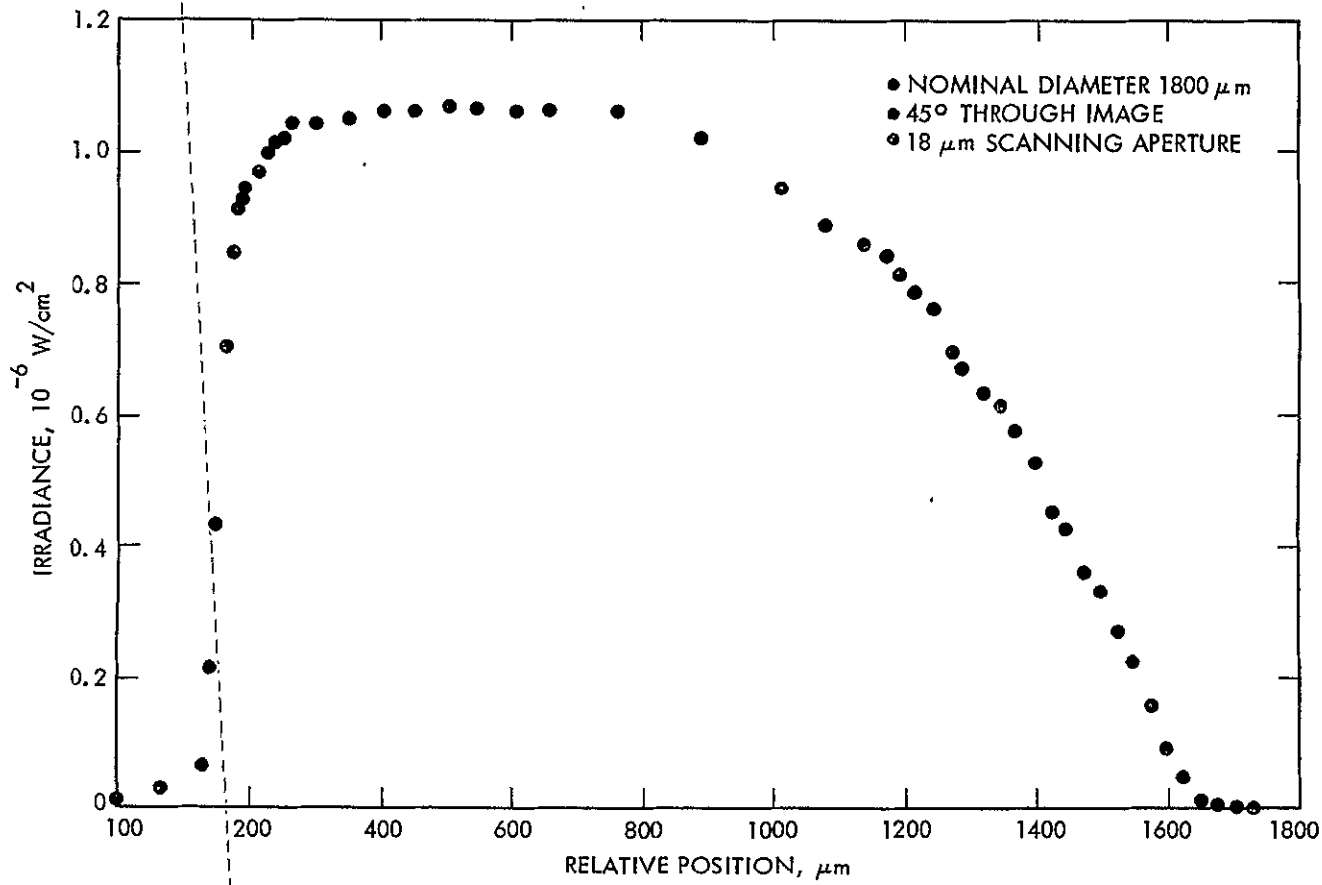


Fig. 22. Image Plane Intensity Traverse for  $30^\circ$  Phase Angle Target

The star profile is of the central core of the image. The shape is close to that which would be expected for the convolution of the central image (within the first minima) with a circular scanning aperture of a similar diameter.

The edge profile of the clear disk image does not exhibit the extreme sharpness of the star core but is consistent with the estimated image quality and is the principal contributor to the optical uncertainty in the relative star/target-body positions.

The 30-deg phase disk profile is from a positive photographic transparency of a 5-cm dental stone sphere illuminated by a collimated Xenon source. A larger (earlier) scanning aperture of 18  $\mu\text{m}$  was used. The transition from dark to limb is shown in the 140 to 180- $\mu\text{m}$  range with the expected brightening towards the subillumination point from 180 to 300  $\mu\text{m}$ . A broad plateau (with some saturation) is exhibited from 300 to 800  $\mu\text{m}$ , and there is Lambertian terminator falloff to 1600  $\mu\text{m}$ .

Figure 23 is a portion of the element printout of the edge of a 150-pixel diameter clear disk at an exposure of 80%. The 4% background adjacent to the top edge of the disk (shown) exhibits a significant darkening, covering 4 to 5 lines, and reaching a drop of the background level of 67% just before the beginning of the disc edge.<sup>4</sup> This is typical of extended targets and illustrates the "line pull" offset of beam bending shown in Fig. 27.

Any instability of the image irradiance translates into apparent position shifts during profiling. This effect was minimized by re-referencing intensities during calibrations, resulting in a total estimated error contribution of less than 0.5  $\mu\text{m}$ .

In total, then, taking the rms of all error sources, the relative 1- $\sigma$  image-location error is 7.0  $\mu\text{m}$  for the effects of both axes.

---

<sup>4</sup> Also seen in the disk profile of Fig. 8 for the top edge (A). The bottom edge (B) shows the inverse effect, the bright edge of the profile overshoots. Right and left edge profiles exhibited little, if any, of either effect. The level offset between the two profiles is dark current shading.

LINE No.	PIXEL No.				
	431				435
419	112	114	108	117	124
	117	128	133	116	128
	108	120	104	105	121
	108	117	114	124	114
	108	109	109	108	106
	91	86	81	83	84
	71	74	78	77	87
	53	33	43	34	33
	289	282	254	190	128
	932	886	852	772	684
	1272	1284	1235	1187	1105
	1542	1551	1543	1462	1408
	1782	1782	1763	1720	1653
	1991	1984	1958	1918	1828
	2155	2146	2137	2090	2037
	2210	2185	2194	2217	2181
435	2242	2210	2235	2204	2214

Fig. 23. Pixel Printout of Top Edge of a Bright Clear Disc (FN100).

#### B. STAR-IMAGE CENTERFINDING ACCURACY

Figure 24 illustrates a star video image at exposure levels of 1.5, 3, 6, and 12%. The four data frames were taken at a format of 500 lines by 500 elements. The average background level was 0.7%,<sup>5</sup> with quantization well into the line-direction noise level of 3.3 DN rms. The typical image size of 2 lines by 2 elements for a threshold star is shown in (a) with image brightness growth in (b), (c) and (d). The peak (element) signal to (line) noise ratio in (a) was 5 to 1, while the integrated net star signal to noise ratio was 13 to 1. These numbers are consistent with the requirement for sufficient optical signal energy to generate the minimum size video image (2 x 2) for subpixel star centerfinding, and with adequate element probabilities of detecting an existing signal (99%) and not detecting a non-existing signal (1%). The centerfinding process requires consideration of the value of each detected element, which is accomplished by the contour processing described below.

<sup>5</sup> Starting at 0.9% in (A) and dropping to 0.5% in (D).

LINE NO.	PIXEL NO.					PIXEL NO.				
	257	261	257	261		257	261	257	261	
384	22 28 18 31	30	19 14 15 24	21		25 24 13 24	24			
	36 32 34 30	29	22 28 42 31	30		22 33 62 43	17			
	21 25 45 31	24	28 26 28 21	22		28 26 28 21	22			
	17 27 41 34	24	14 21 12 20	21		14 21 12 20	21			
	22 26 24 30	26	27 22 17 17	23		27 22 17 17	23			
390	34 34 26 24	31								
	27 28 19 20	29								

(a) 1.5% EXPOSURE  
(FN 76)

(b) 3% EXPOSURE  
(FN 77)

LINE NO.	PIXEL NO.					PIXEL NO.				
	257	261	257	261		257	261	257	261	
384	14 15 8 8	13	22 22 20 20	17		18 31 33 28	18			
	21 16 15 11	14	18 124 319 154	30		22 127 394 233	27			
	17 47 117 59	19	22 127 394 233	27		14 27 56 39	17			
	11 51 167 99	17	14 27 56 39	17		16 17 20 14	13			
	20 24 30 22	13	16 17 20 14	13		14 3 16 12	10			
390	15 15 12 8	16								
	19 20 12 14	13								

(c) 6% EXPOSURE  
(FN 79)

(d) 12% EXPOSURE  
(FN 80)

Fig. 24. Pixel Printouts of a Typical Star as a Function of Intensity

Four star-field test frames were taken on the simulator to measure the amount of offset caused by increasing star-exposure levels. A fixed field of 10 stars of the same relative intensities was set up. An exposure time of 6 s was used for each frame. The star scale was varied from 2% to 75% by means of the zoom illuminator control. A flood erase camera cycle resulting in a 4% background was used. The star scale used here (as elsewhere) was determined by setting the peak video level at 50% of full scale, and referencing all exposures to this (i.e., a 25% star scale means that the star illumination level was half that of the 50% reference). The test frames were recorded in succession (after a four-hour camera warmup) and contour plots of all star locations were then run on the 1108. A sample set of contour plots is shown in Fig. 25. Manual centerfinding was performed on all 40 star-image contours as follows: one center was found at 2% exposure, two centers (at a high and a low contour) were found at 7% exposure, and four

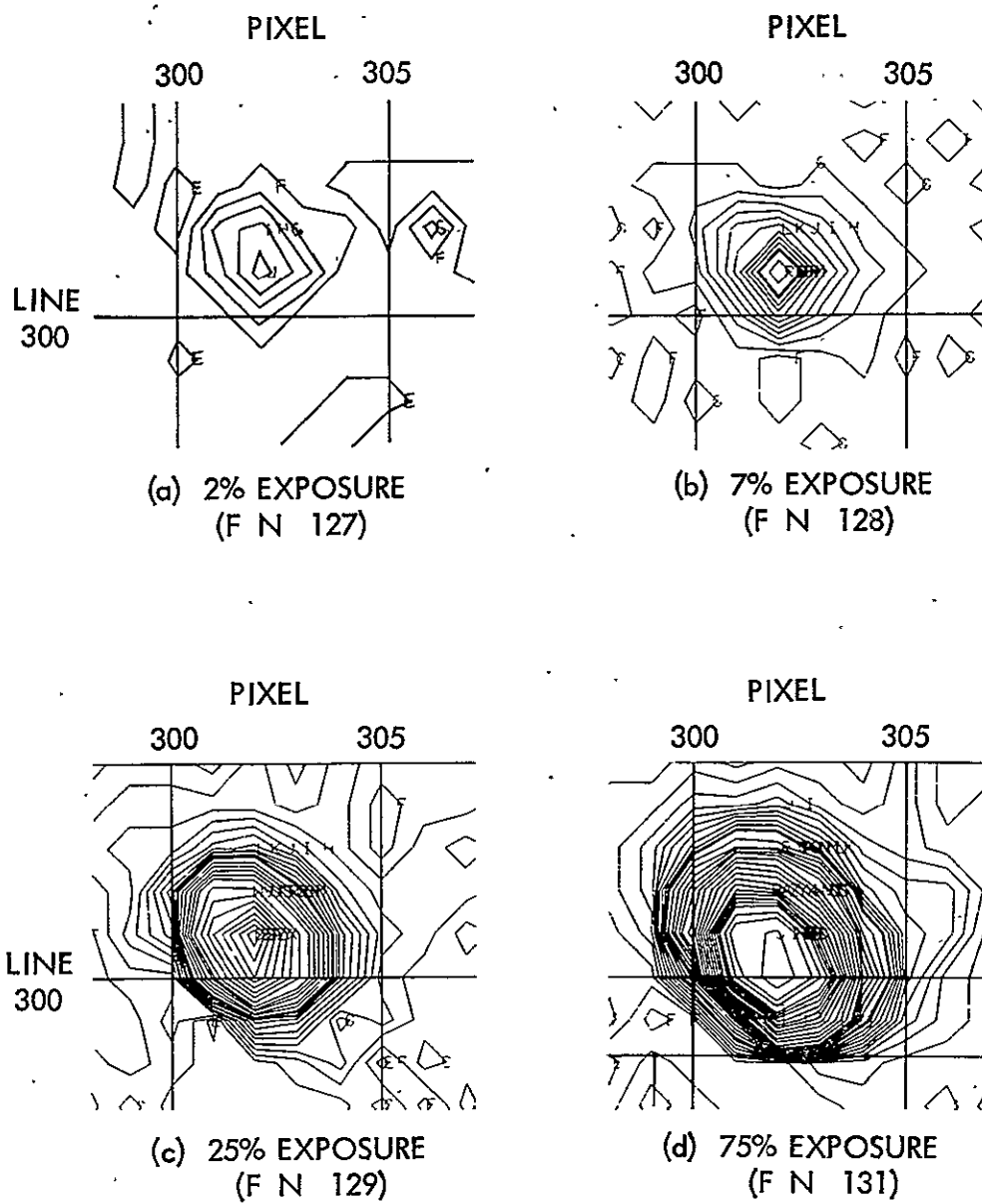


Fig. 25. Contours of a Typical Star as a Function of Intensity

levels (high, medium, intermediate, and low contours) were found at both 25 and 75% exposures. The contour centerfinding was done by "boxing-in"<sup>6</sup> the contour of interest and measuring the centroid of the box to 0.01-pixel. The results for the sample are shown in Table 1.

Table 1. Sample star-image centerfinding results

Contours	Exposure							
	2%		7%		25%		75%	
	Line	Pixel	Line	Pixel	Line	Pixel	Line	Pixel
Low	---	---	301.11	297.00	301.05	297.01	301.15	297.10
Intermediate	---	---	---	---	300.85	296.99	301.15	297.10
Medium	301.35	297.01	---	---	300.92	296.96	300.70	297.00
High	---	---	301.01	297.11	300.82	296.96	300.50	296.89

The 2% exposure position was used as a reference and subtracted from all of the centroids to determine the relative shift with increasing exposure. All of the pixel differences were then averaged (at a given exposure level), and then the line differences were likewise averaged and plotted in Fig. 26. The pixel direction average shifts were all within 0.07 pixels and do not show a trend. However, the line direction average shifts show an increasing negative offset with increasing exposure to a maximum of 0.27 elements. The average of all stars at each level was plotted in Fig. 27 showing the offset trend as a family of curves for different contour levels. The results show that the largest offsets (up to 0.45 lines) occur when the high contour is used (generally one down from the top) and the smallest offsets (less than 0.1 lines) occur when the low contour (the lowest that is well defined) is used.

---

<sup>6</sup> Drawing a rectangular box that included about 75% of the area of the contour through the contour.

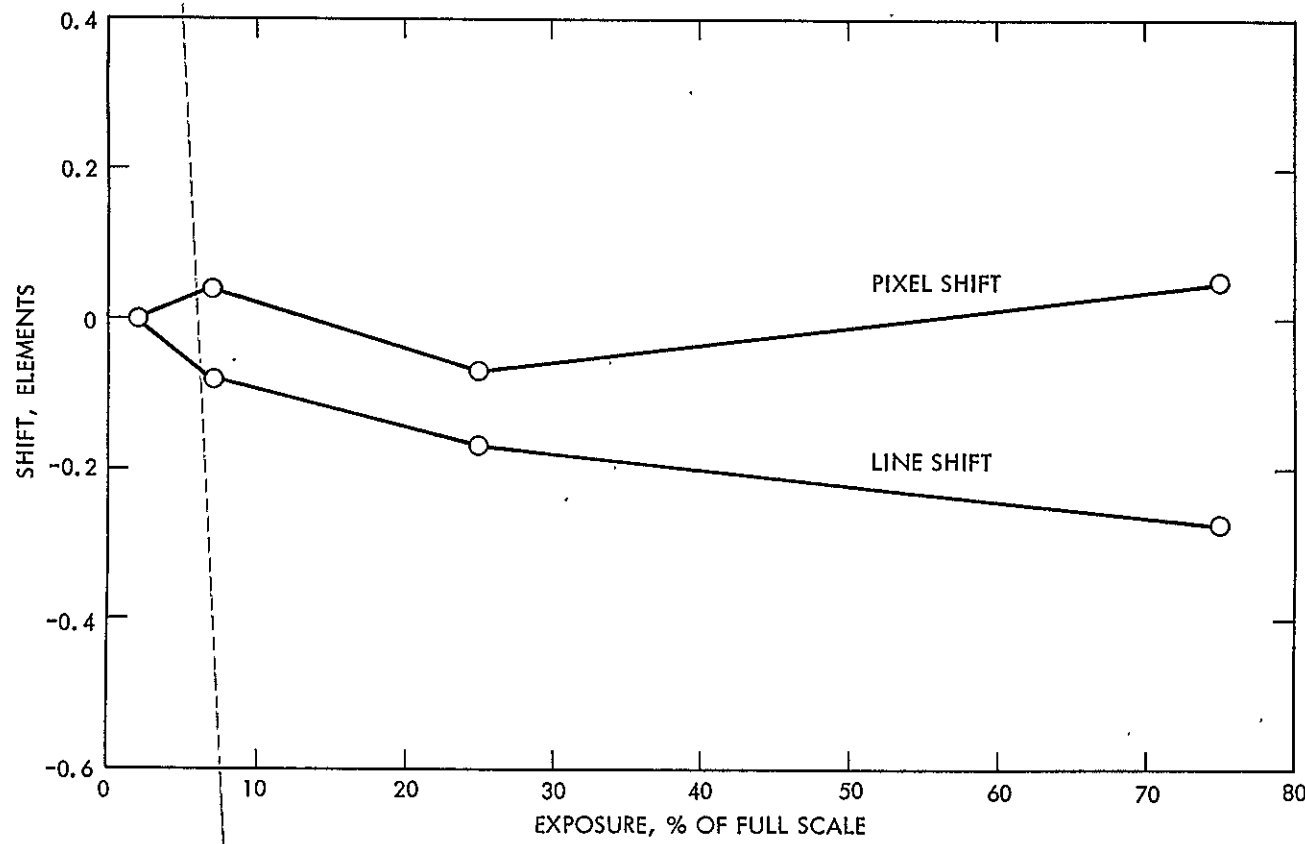


Fig. 26. Star Image Motion vs Brightness

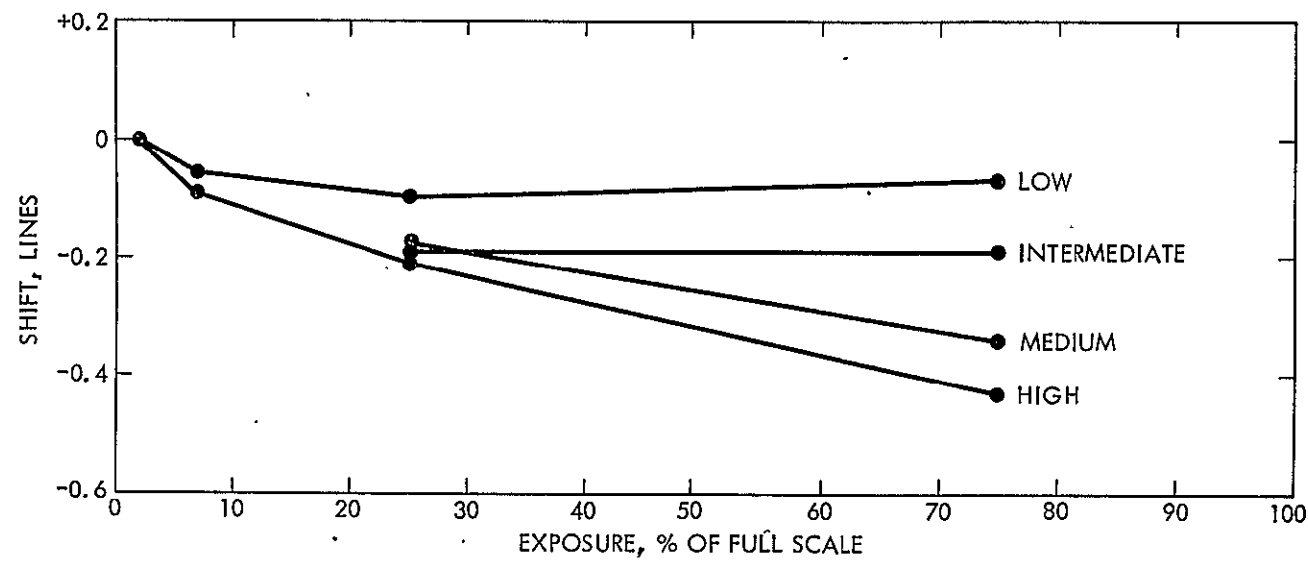


Fig. 27. 4-Level Line Offset vs Star Brightness

### C. TARGET/STAR MEASUREMENT

Perhaps the most important goal of the vidicon test program was the quantitative evaluation of target/star measurement errors for simulated optical navigation scenes. It was recognized early in the development of optical navigation technology (Ref. 7) that difficulties might be encountered in obtaining target/star measurements for future missions, particularly where the target image is very much brighter than the surrounding stars. Since then, the ability of flight cameras for imaging faint background stars, down to visual magnitude 9, has been demonstrated (Ref. 3, 4). It was also demonstrated that measurements of a large bright target and background stars could be made consistently repeatable to the one-pixel level.

However, it has not been possible to accurately determine systematic measurement errors using flight data. Fixed biases, or errors which vary slowly with image geometry, can seriously affect navigation accuracy. For example, a small systematic measurement error that varies with illumination phase angle might be incorrectly attributed to the orbital parameters of a satellite, resulting in substantial satellite-relative trajectory errors. Similar variations with image size or brightness are also possible.

For this reason, an attempt was made to determine systematic target/star measurement errors in the laboratory. Initial plans called for error characterization versus image size, brightness, phase angle, position in the field of view and albedo variations. However, funding limitations, combined with a new emphasis on solid-state imaging sensors for missions beyond MJS'77, led to a reduction in vidicon program scope. The primary program goals were redirected to determining bias errors for a fixed geometry scene over a wide range of illumination. Measurements were made with a "clear disk" target to simplify measurement procedure and lessen dependence-on-software variation.

Measurement results are summarized in Figs. 28, 29, 30. Image offsets, displayed in these figures, are defined as the difference in the location of the disk image between that measured using vidicon data and that determined by geometric calibration of the optical image. Both measurements, optical and video, are referenced with respect to star images within the frame. This procedure is consistent with flight optical navigation measurements, where

disturbances affecting star and target images equally (such as camera-pointing errors) are unimportant. On the other hand, error sources affecting each image differently, such as electron-readout beam bending, can produce systematic measurement errors. These effects appear as image offsets in the figures.

Figure 28 shows measured image offset in the line direction versus exposure for a 150-pixel disk image. The center of the video image was found using a standard two-dimensional limbfit procedure (as described previously) based on the limb points selected near peak video intensity of the limb (Fig. 8, Level III). Several general features of Fig. 28 deserve comment. At very low exposures (less than 10% of full scale), the image has shifted by more than one TV line (toward lower line numbers) with respect to its expected location. As observed, this shift corresponds to a sizable fixed-measurement bias.<sup>7</sup>

As the exposure is increased toward full scale (image exposure = 1.0), the line offset increases from approximately one to two TV lines. The calibration uncertainty mentioned above does not affect measurement of this trend, since the relative data accuracy is approximately +0.1 line. Note that, after the target is exposed to approximately full scale, further exposure results in negligible changes in the line offset, until very large exposures (>30X) are reached.

The trend of the changes displayed in Fig. 28 can be qualitatively explained in terms of electron-beam bending effects. The vidicon readout beam is attracted by regions on the vidicon target which are the most positively charged. This effect causes bright target images to be sensed before (i.e., at lower line number) they would be detected with perfect readout. Thus, when the target brightness increases between 0.05 and 1.0 times full scale, the beam deflection and image offset increase accordingly. When saturation is reached, further increases in intensity have little effect on the image and, therefore, on the center location.

---

<sup>7</sup> The influence of the microradiometer calibration of the simulated image on the results is discussed below.

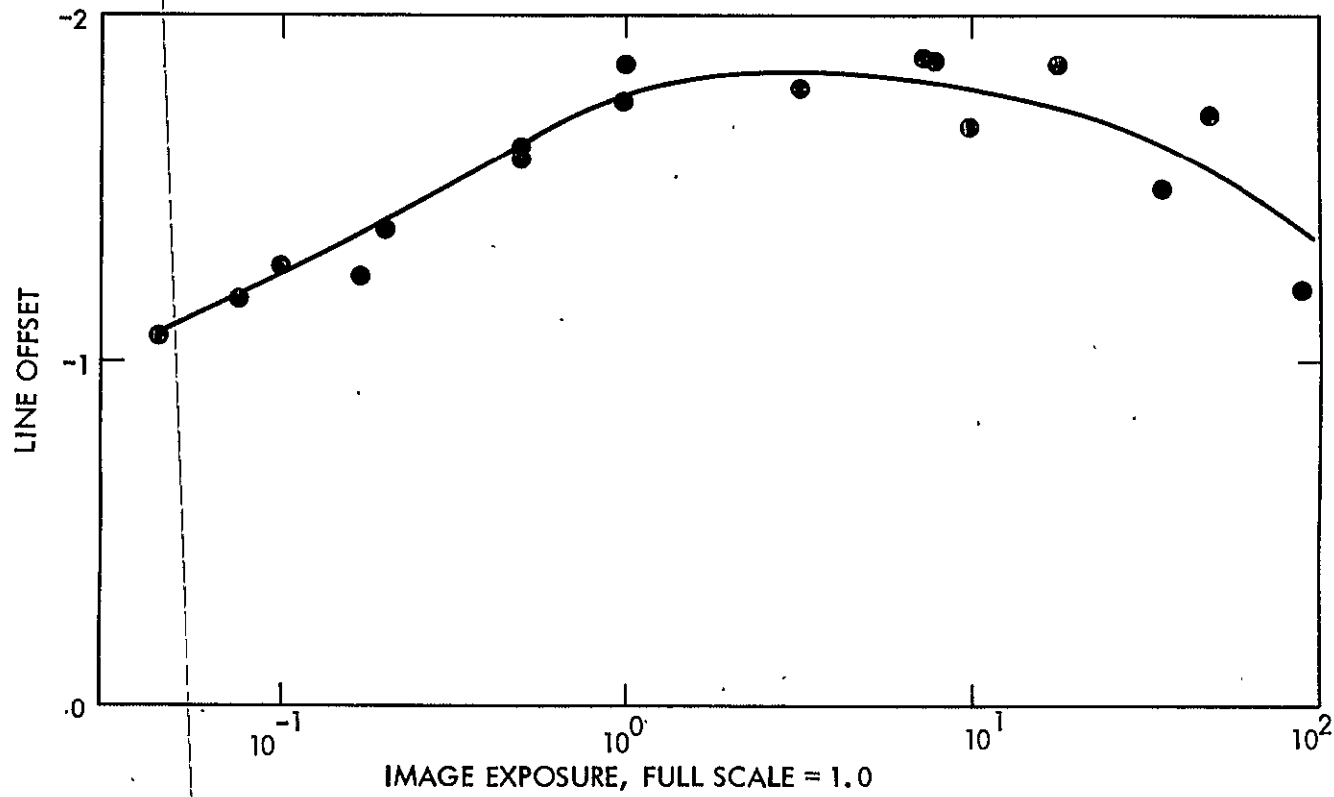


Fig. 28. Target Body Motion vs Exposure (Target center found using "high" intensity contour (Section II))

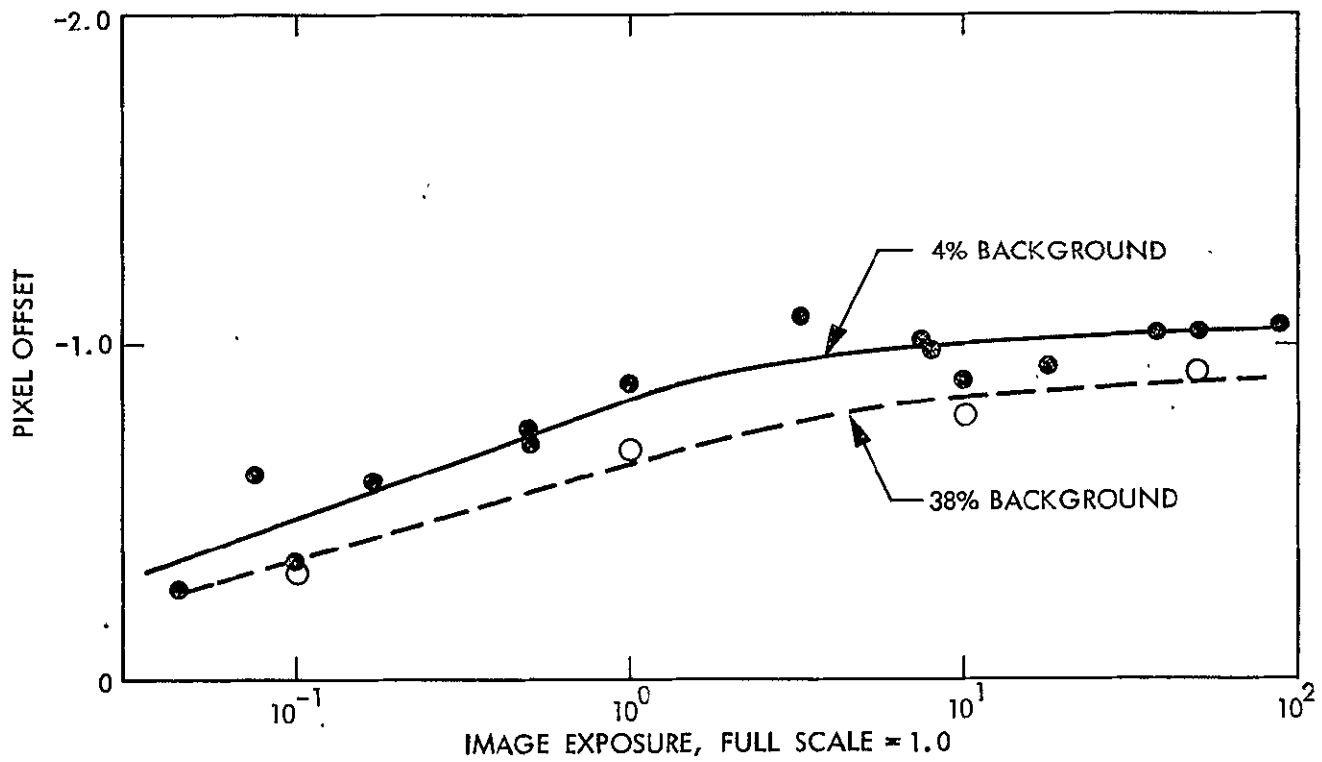


Fig. 29. Target Body Motion vs Exposure (pixel direction)

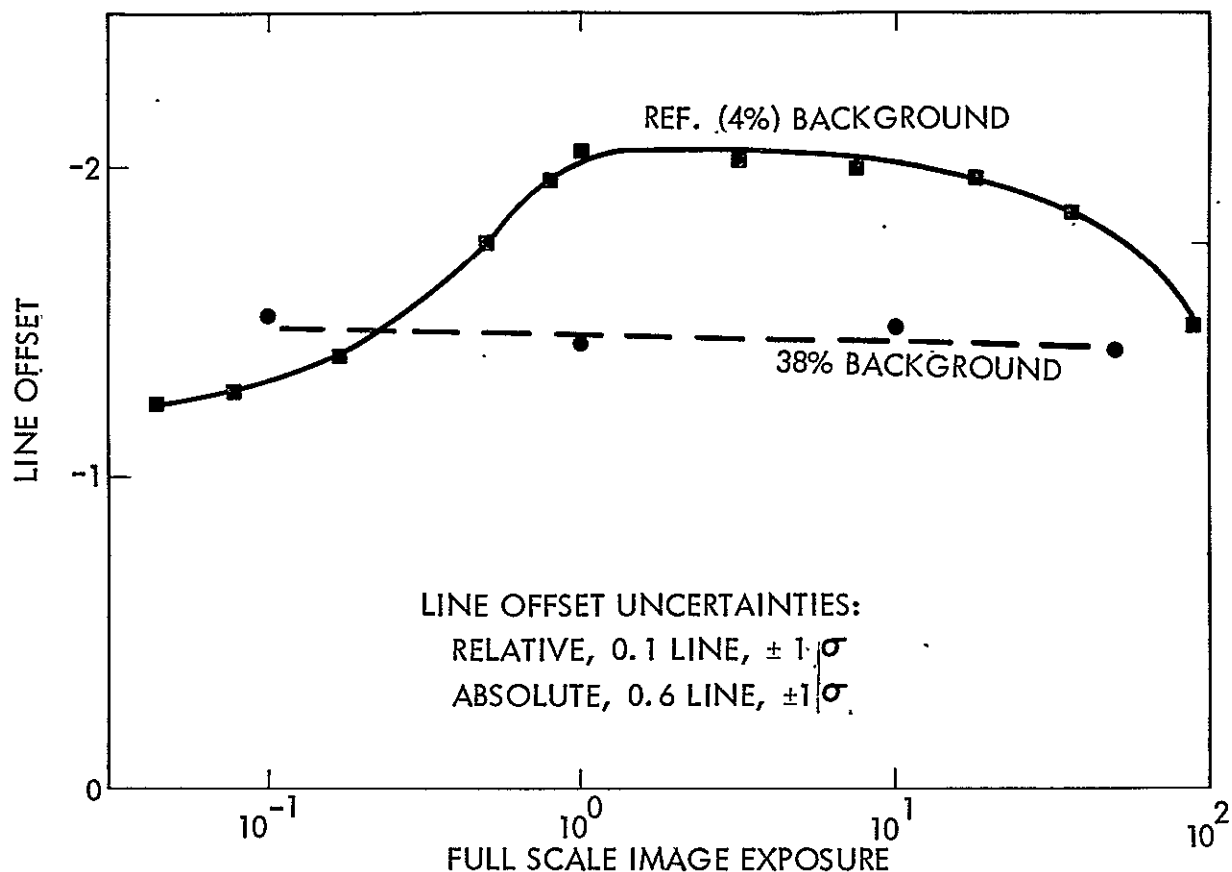


Fig. 30. Target Body Shift vs Exposure (Low contours)

However, as the exposure is increased to the point where image flare becomes important, two effects seem to emerge. First, scattered light from the target image increases the readout beam bending for star images, resulting in star image shifts which partially offset the target body shift. Secondly, the limbfitting process itself is increasingly affected by scattered light. The resulting image center more nearly reflects the center of the scattered light (optical flare) distribution and not the true limb. This effect could become very significant at larger phase angles, where the optical flare becomes increasingly asymmetrical.

Figure 29 again shows the image offset in the line direction, this time based on limb points derived from a lower video intensity (Level II, Fig. 8). A slightly higher offset is associated with the lower value, but in general the lower threshold is preferred, because of improved limb-point definition.

Also plotted are the image shifts measured in the presence of a 38% background light flood. Previous results have shown (Ref. 4) that optically raising the video background (dark) level can increase the detectability of very faint star images. It was suspected that this added background might also lessen the effects of beam bending since the image charge gradient at the limb would be lowered. As can be seen in Fig. 29, this is indeed the case. The image shift is essentially constant over nearly three orders of magnitude of exposure and corresponds to the offset measured with a very low ( $\sim$ 20% full scale) dark-field image exposure.

Figure 30 gives similar offsets in the pixel (sample) direction. Neither effect noted in the line direction applies here. Measured offsets, although tending to stabilize for saturated exposures, show no sign of reversal even at exposures as high as 90 times full-scale, nor does background light flooding eliminate the exposure dependence as it does in the line direction. It merely reduces the offset by approximately 0.2 pixel.

The general character of trends appearing in Figs. 28-30 can be clarified by examining the behavior of vidicon reseaux. Fig. 31 illustrates reseau motion because of a heavily overexposed target body image. The two reseau marks interior to the target image are displaced toward lower line values by between one and two pixels. Marks outside of the image, in general, show a similar displacement, particularly those directly above the bright disk. These motions are typical for a heavily overexposed disk image and reflect electron-beam bending of a bright target image and the associated optical flare.

Figure 32 graphically demonstrates the value of a partial background light flooding. The light flooding tends to even out beam bending over the entire frame, making reseau image locations less sensitive to the presence of bright target image.

The displacements plotted in Figs. 31 and 32 were derived by subtracting reseau locations measured in a dark-field frame from locations measured when the target-straylight images are projected.

Most of the pattern irregularities visible in Fig. 32 are due to measurement inaccuracies for the dark-field frame. With no added background, reseau images are weak and noisy (Fig. 33). Centerfinding errors for these images

Fig. 31. Reseau Motion Due to Heavily Overexposed (50x) Disk Image (Normal background level)

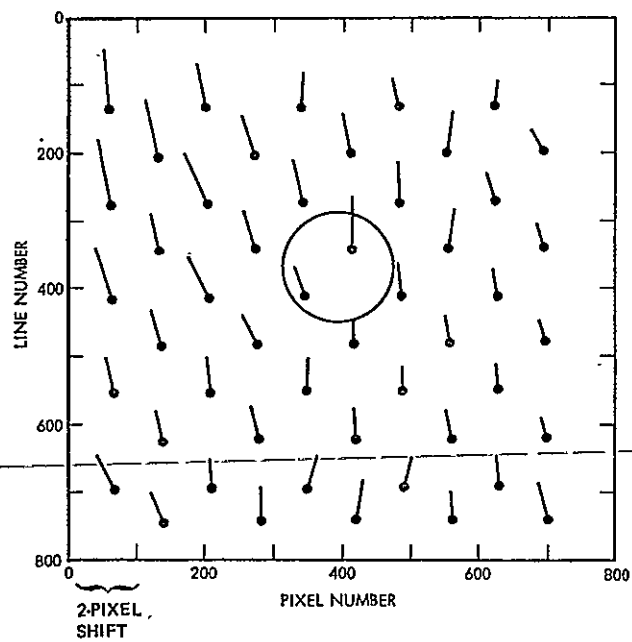
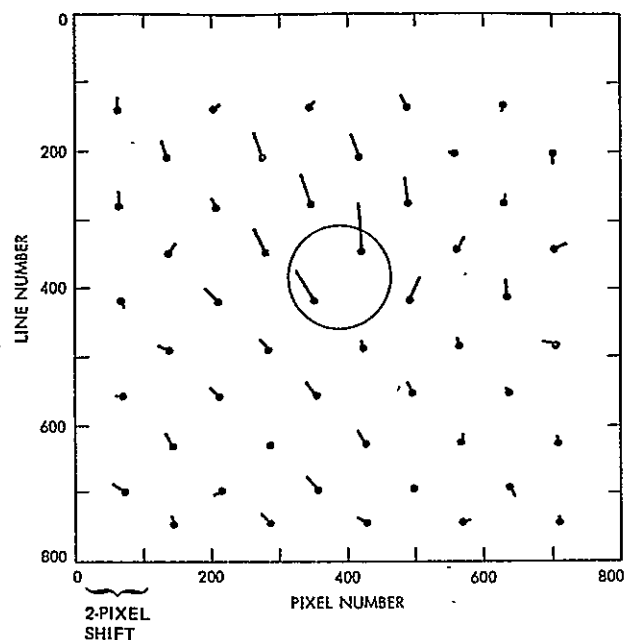


Fig. 32. Reseau Motion Due to Heavily Overexposed (90x) Disk Image with 38% Background Light Flood

were typically 0.2 pixels ( $1\sigma$ ). However, even a 10% background light level (Fig. 34) dramatically improved reseau visibility, resulting in better than 0.1-pixel centerfinding accuracy for frames with partial background light flood.

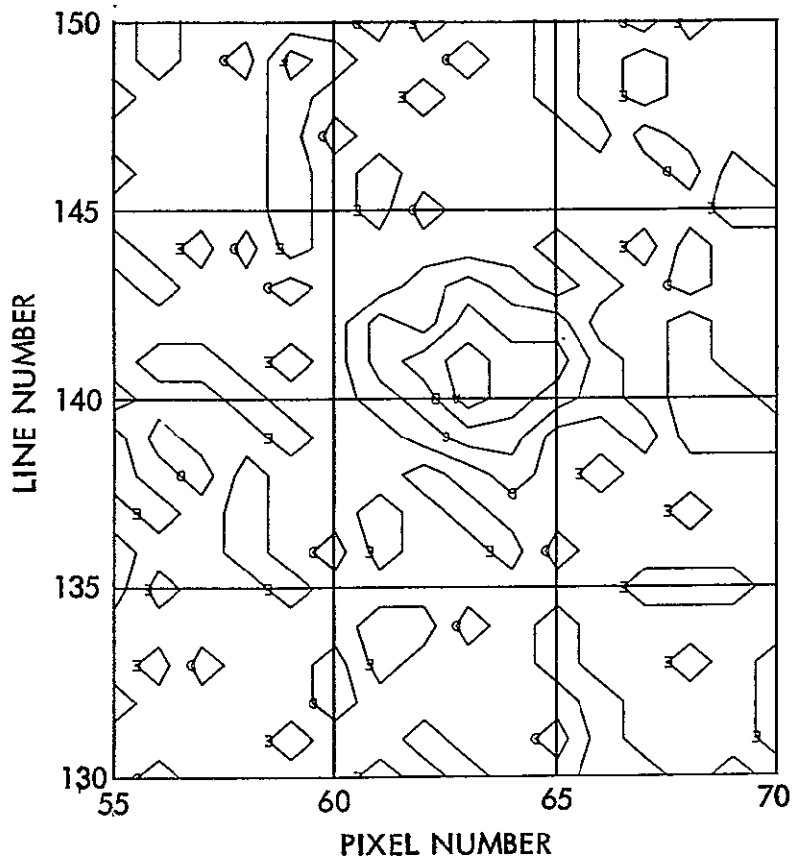


Fig. 33. Typical Reseau Image Against Weak Background

An interesting comparison can be made between the motion of reseau images and the motion of the bright disk image as a function of exposure (Fig. 35). Both image types display a similar behavior except for the large "zero offset" of the clear-disk center measurements (at the low exposure limit). Unfortunately, it was not possible to make an independent optical determination of reseau locations with respect to star images. Thus, no absolute measurement of zero offset is possible for reseaux. However, it seems reasonable to assume that very weak reseau images behave the same way as very weak star images.

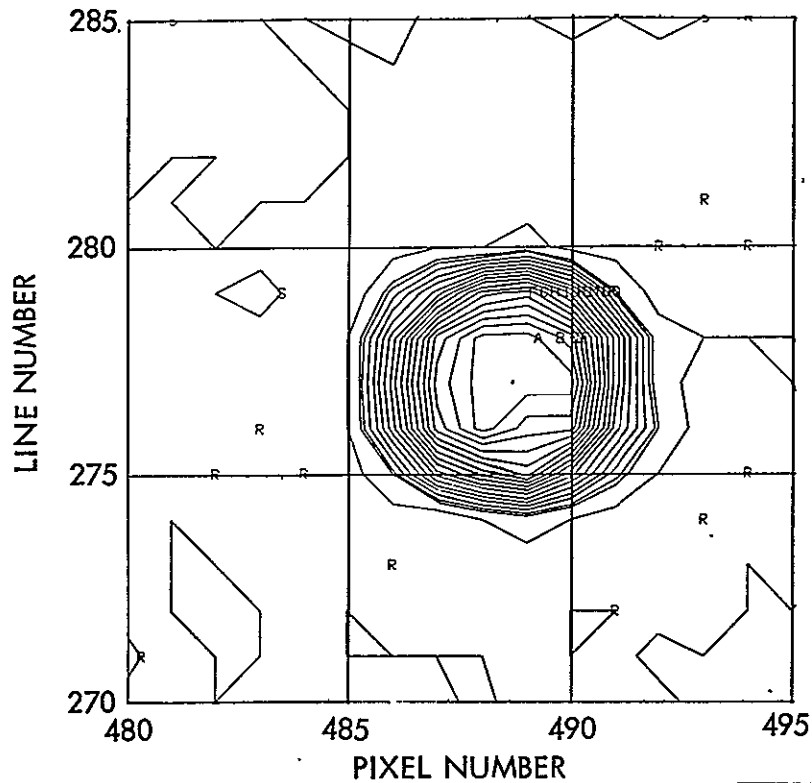
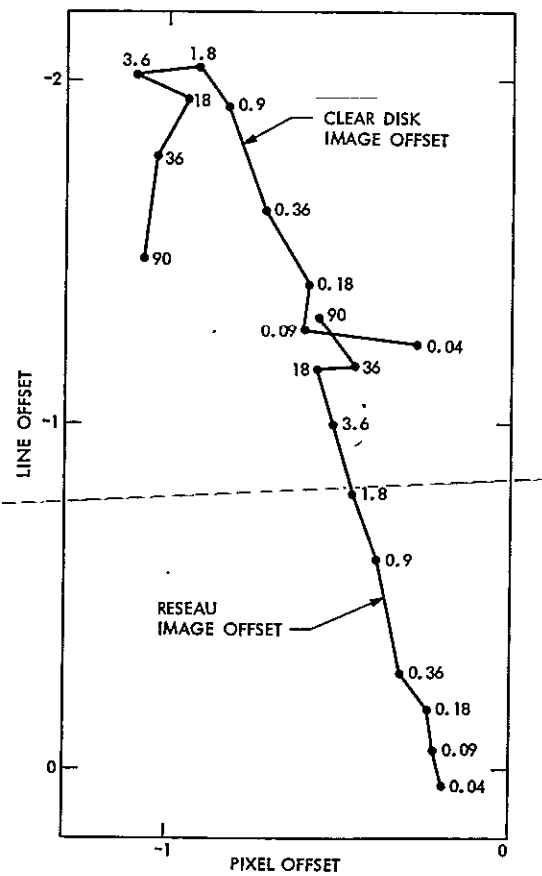


Fig. 34. Reseau Image with 10% Background Light Flood

Fig. 35. Reseau and Disk Image Motion vs Exposure (Exposure is indicated as fraction of full scale - Reseau motion is average of two reseau inside disk image).



Since star images provide the bench marks for all optical measurements, this assumption is equivalent to a negligible "zero offset" for reseaux. Thus, the data in Fig. 35 suggest that, while a reseau location shifts slowly with background level for weak exposures, the disk image displays an image offset in excess of one TV pixel even for very weak exposures.

It should be noted that the measured offsets are approximately 2 times greater than the  $1-\sigma$  simulator position calibration uncertainty of 0.6 elements ( $7 \mu\text{m}$ ). However, the conclusion stands that beam bending offsets of large disks are important at all exposure levels. More extensive tests, particularly simulating a range of phase angles, are needed to confidently apply these results to a flight situation.

#### D. SUMMARY

A limited set of laboratory tests have been conducted to investigate significant vidicon-related optical-measurement parameters. Factors affecting center location measurements for star, reseau, and extended target images were explored. Although calibration uncertainties still affect the measurement of fixed-bias offsets, exposure-dependent variations were measured to an accuracy of approximately 0.1 pixel.

Important results were derived in the following general areas:

- (1) It was demonstrated that star image centerfinding accuracy is a function of both the image brightness and the intensity contour used in centerfinding. Selection of low-level contours results in image displacements of less than 0.1 pixel over the linear range of vidicon response.
- (2) Target body image offset generally increases ( $\sim 3/4$  pixel and line) with exposure, until saturation is reached. After this point, there is little change with exposure until image flare effects become significant.
- (3) Image flare affected laboratory measurements only at very large overexposures (50X or more). Two factors help explain the apparent image offset turnaround at very high exposures (Fig. 28). First, the increased straylight throughout the frame caused some motion of measured location for star images. Secondly, flare asymmetry around

the bright target began to influence limb-point measurement. The latter effect could be important for higher phase angles, where image flare is strongly asymmetrical.

- (4) Although reseau marks can be detected on a very low video background (1% of full scale), the attainable measurement accuracy is substantially improved by a modest (4 to 10%) increase in background level.
- (5) Finally, partial background light flooding was shown to be a powerful technique for improving optical-navigation measurement accuracy by reducing the effects of electron-beam bending and increasing the visibility of black-sky reseau marks. These benefits, when combined with the increased sensitivity to stars previously demonstrated, point strongly to the use of partial light flooding for all vidicon-based, optical-navigation measurements.

SECTION VI  
DIRECTIONS FOR FUTURE WORK

Field and laboratory tests reported here have answered some of the concerns relating to the application of Mariner vidicons to optical navigation. Other concerns remain largely unanswered. Among these is the calibration of image-offset errors versus phase angle and target-image size. This calibration should probably be conducted using flight hardware and calibrated test images which match, as nearly as possible, actual mission geometry. Since the optical measurement reflects both the hardware characteristics and the software used for data extraction, instrument calibrations should apply the same algorithms (limb-point extraction, centerfinding techniques, etc.) that will be used in flight.

Solid-state imaging sensors may replace vidicons for optical navigation imaging on future missions. Since these sensors do not suffer beam bending and other vidicon-related distortions, the potential exists for a substantial increase in measurement accuracy. This fact, combined with the greater sensitivity and dynamic range of solid-state sensors, supports the need for optical-navigation, experimental-performance evaluation.

A sensor program is being pursued to study the applicability of solid-state imaging sensors to autonomous guidance and navigation. This application combines the improved performance of solid-state sensors with simplified measurement extraction algorithms, implemented in an associated microprocessor, to derive target/star measurements on board a spacecraft. The development and testing of this technology will apply many of the simulations and techniques already developed for the work described here.

REFERENCES

1. Duxbury, T. C., and Breckenridge, W. G., "Mariner Mars 1969 Optical Approach Navigation," AIAA Paper 70-70, New York, January 1970.
2. Breckenridge, W. G., and Acton, C. H., "A Detailed Analysis of Mariner 9 TV Navigation Data," AIAA Paper 72-866, Stanford, California, 1972.
3. Born, G. H., et al, Mariner Mars 1971 Optical Navigation Demonstration--Final Report, Technical Memorandum 33-683, Jet Propulsion Laboratory, Pasadena, California, April 1974.
4. Stanton, R. H., Ohtakay, H., and Miller, J. A., "Demonstration of Optical Navigation Measurements on Mariner 10," AIAA Paper 75-86, Pasadena, California, January 1975.
5. Acton, C. H., and Ohtakay, H., "Mariner-Venus-Mercury Optical Navigation Demonstration: Results and Implications for Future Missions," AAS Paper 75-088, Nassau, Bahamas, July 1975.
6. Breckenridge, W. G., General Design Document for Optical Measurement Set (OMSET)--Viking 75 Project, Report 620-112, Jet Propulsion Laboratory, Pasadena, California, October 1973 (an internal document).
7. Stanton, R. H., "Challenges in Developing an Approach Guidance Instrument for the Outer Planets," AAS Paper 71-119, Seattle, Washington, June 1971.

PRECEDING PAGE BLANK NOT FILMED

APPENDIX A

TEST-SET OPERATIONAL CONTROLS

*PRECEDING PAGE BLANK NOT FILMED*

All test-set operational controls described in this appendix were push-button, unless otherwise specified.

- (1) EXPOSURE: A seven-segment, decimal digi-switch (with countdown LED display) with a range from zero to 99 min. and 59.999 s. Setting is recorded in frame header and retrace block.
- (2) FRAME ID: A three-segment, decimal digi-switch. A pushbutton inputs the setting to the frame counter, which advances by one count at the end of each frame. Frame number is recorded in frame header and retrace block.
- (3) FORMAT: A three-segment, decimal digi-switch. The range is from 250 x 250 to 999 x 999 lines by pixels. Recorded as one and two.
- (4) STOP: Terminates any operation or cycle.
- (5) AUTO: Initiates automatic cycling consisting of the following:
  - (a) Preparatory vidicon erase cycle.
  - (b) Exposure.
  - (c) Ten second settling time.
  - (d) Vidicon read/tape write.
  - (e) Flood.
  - (f) Erase cycle.
  - (g) Stop.
- (6) EXPOSE: Initiates expose cycle with 10-s settling time.
- (7) WRITE: Initiates vidicon read and tape write.
- (8) ERASE: Initiates erase cycle consisting of 14 scans, at higher target voltage, in one frame-time. Starts with a 2-s flood.
- (9) TAPE WRITE INHIBIT: Inhibits tape-write cycle during vidicon read.
- (10) FLOOD INHIBIT: Inhibits flood during erase.
- (11) IRG INHIBIT: Inhibits generation of inter-record gaps during tape write.
- (12) FILAMENT AUTO/ON: Places vidicon filament in automatic cycle for exposures longer than 30 s.

APPENDIX B

FIELD-TEST FRAMES

~~PRECEDING PAGE BLANK NOT FILMED~~

The field-test frames are:

FRAME #	EXPOSURE	TARGET
1	1 s	Test frame
2	4 s	Saturn
3	4 s	Saturn
4	6 min	Comet Bradfield
5	10 min	Comet Bradfield
6	1 s	Gamma Leo
7	1 s	Gamma Leo
8	2 min	M67-Open Star Cluster
9	30 s	M67-Open Star Cluster
10	2 min	M3-Globular Star Cluster
11	10 min	M3-Globular Star Cluster
12	5 min	Comet Bradfield
13	5 min	Comet Bradfield
14	10 min	Comet Bradfield
15	10 min	Comet Bradfield
16	5 s	Castor (not tracked)
17	30 s	M44-Open Star Cluster
18	5 min	M94
19	0.25 s	Saturn
20	1 s	Saturn
21	5 s	Saturn
22	2 min	Saturn
23	4 min	Saturn
24	1 s	Mars
25	0.2 s	Mars
26	0.5 s	Mars
27	0.2 s	Moon
28	0.6 s	Moon
29	1 min	Moon, straylight
30	20 s	M67

PRECEDING PAGE BLANK NOT FILMED

31	1 min	M67
32	2 min	M67
33	4 min	M67
34	10 min	M67
35	5 min	Comet Bradfield
36	2 min	Comet Bradfield
37	1 min	Comet Bradfield
38	6 min	Comet Bradfield
39	1 min	Stars (Corvus)
40	20 s	Stars (Corvus)
41	6 s	Stars (Corvus)
42	2 s	Stars (Corvus)
43	1 s	Stars (Corvus)
44	4 s	Stars (Corvus)
45	3 s	Uranus
46	3 s	Uranus
47	1 s	Uranus
48	3 min	Uranus
49	1 s	Star ( $\tau_6$ Ser)
50	2 s	Star ( $\tau_6$ Ser)
51	2 s	Star ( $\tau_6$ Ser)
52	2 s	Star ( $\tau_5$ Ser)
53	2 s	Star ( $\tau_2$ Ser)
54	2 s	Star (12 Ser)
55	2 s	Star (12 Ser)